

1-31-1991

A multimode index detecting sensor for use in plastic concrete

Qiyu Chen
New Jersey Institute of Technology

Follow this and additional works at: <https://digitalcommons.njit.edu/theses>



Part of the [Electrical and Electronics Commons](#)

Recommended Citation

Chen, Qiyu, "A multimode index detecting sensor for use in plastic concrete" (1991). *Theses*. 2455.
<https://digitalcommons.njit.edu/theses/2455>

This Thesis is brought to you for free and open access by the Electronic Theses and Dissertations at Digital Commons @ NJIT. It has been accepted for inclusion in Theses by an authorized administrator of Digital Commons @ NJIT. For more information, please contact digitalcommons@njit.edu.

Copyright Warning & Restrictions

The copyright law of the United States (Title 17, United States Code) governs the making of photocopies or other reproductions of copyrighted material.

Under certain conditions specified in the law, libraries and archives are authorized to furnish a photocopy or other reproduction. One of these specified conditions is that the photocopy or reproduction is not to be “used for any purpose other than private study, scholarship, or research.” If a user makes a request for, or later uses, a photocopy or reproduction for purposes in excess of “fair use” that user may be liable for copyright infringement,

This institution reserves the right to refuse to accept a copying order if, in its judgment, fulfillment of the order would involve violation of copyright law.

Please Note: The author retains the copyright while the New Jersey Institute of Technology reserves the right to distribute this thesis or dissertation

Printing note: If you do not wish to print this page, then select “Pages from: first page # to: last page #” on the print dialog screen

The Van Houten library has removed some of the personal information and all signatures from the approval page and biographical sketches of theses and dissertations in order to protect the identity of NJIT graduates and faculty.

A Multimode Index Detecting Sensor For Use In Plastic Concrete

by

Qiyu Chen

Thesis submitted to the Faculty of the Graduate School
of the New Jersey Institute of Technology in partial fulfillment
of the requirements for the degree of
Master of Science in Electrical Engineering

1999

Approval Sheet

Title of Thesis: A Multimode Index Detecting Sensor For Use In Plastic Concrete

Name of Candidate: Qiyu Chen
Master of Science in Electrical Engineering, 1990

Thesis and Abstract Approved: _____
Dr. Farhad Ansari Date
Associate Professor
Department of Civil Engineering

Dr. Gerald Martin Whitman Date
Professor
Department of Electrical Engineering
Director
Center for Microwave and Lightwave Engineering

Dr. Edip Niver Date
Associate Professor
Department of Electrical Engineering

VITA

Name: Qiyu Chen.

Permanent address:

Degree and date to be conferred: M.S.E.E., 1990.

Date of birth: .

Place of birth:

University attended	Dates	Degree	Date of Degree
China Textile University, China	1979-83	B.S.E.E.	July, 1983
New Jersey Institute of Technology	1989-90	M.S.E.E.	December, 1990

Major: Electrical Engineering

To my parents, and to my grandparents.

Acknowledgements

Mere words are not enough to express my gratitude to my advisor, Dr. Farhad Ansari. His mastery of the subject matter combined with a great deal of sincerity and enthusiasm, made working on this thesis a wonderful experience.

Many thanks are due to the distinguished members of my committee: Dr. Gerald Martin Whitman and Dr. Edip Niver. Their suggestions and stimulating discussions have considerably improved the quality of the thesis.

I would also like to thank Dr. Sam Yang, who has made me love computers and for giving me invaluable suggestions.

Last but not the least, I would like to thank my family. Many thanks also go to my parents, for their deep love and encouragement.

Abstract

Title of Thesis: A Multimode Index Detecting Sensor For Use In Plastic Concrete

Name: Qiyu Chen, Master of Science in Electrical Engineering, 1990

Thesis directed by: Dr. Farhad Ansari

This thesis describes a microcomputer-based measuring system using a laser diode source, a fiber optic sensor and a microcomputer DMA interface to test and analyze the entrained percentage of air in concrete.

The principle of refraction and reflection of light in optical fibers is applied to detection of air bubbles. Reflected light intensity signals are detected and transferred through a DMA interface to a laptop computer. Analysis of reflected light intensity produces a measurement of the air content of fresh concrete. Accuracy of the system is evaluated through extensive laboratory and field trials.

Contents

Abstract	iv
Dedication	ii
Acknowledgements	iii
1 Introduction	1
1.1 Air Content in Concrete	1
1.2 Fiber Optic Sensors	2
1.3 Optical Sources	5
1.4 Laser Beam Characteristics	5
1.5 Light Sensing Elements	6
2 System Structure and Principle	10
2.1 Measuring Methodology	10
2.2 System Structure and Basic Components	12
2.3 System Fiber Optic Sensor Structure and Principle	15
2.4 Laser Diode	22
2.5 Laser Diode Control and Drive Circuit	22
2.6 Laser to Fiber Source Coupler	25
2.7 Multimode Fiber Directional Couplers	25

2.8	Photodetector and Operational Circuit	25
2.9	Analog Amplifier and Filter	26
2.10	Data Acquisition System and Microcomputer	31
3	Optical Data Signal Processing	35
3.1	System Operation	35
3.1.1	Signal Flow Operations	37
3.1.2	Signal Analysis	40
3.2	Signal Frequency Analysis	47
3.2.1	Calibration Method	48
4	Experimental Results and Discussion	58
4.1	Experiment Sampling and Testing	58
4.2	Laboratory Results	59
4.3	Field Trials	59
4.4	Air Bubble Numbers and Size Analysis	66
4.5	Conclusions	84
	Bibliography	85
A	Laser Diode Technical Data	87
A.1	TOLD-9200 Features	87
A.2	PIN Connection	87
A.3	Maximum Ratings	87
A.4	Optical-Electrical Characteristics	87
B	Laser Diode Control and Drive Circuit	90
B.1	Laser Diode Control and Drive Circuit	90

B.2	Circuit Devices List	90
C	Laser to Fiber Source Coupler Operation Principle	93
D	Photodetector AF65-R2F Technical Data	95
D.1	Features	95
D.2	Absolute Maximum Ratings	95
D.3	PIN Connection	95
D.4	Electro-Optical Characteristics	97
E	Analog Amplifer and Filter Circuit	98
E.1	Analog Amplifer and Filter Circuit	98
E.2	Circuit Devices List	98
F	Program List	101
F.1	Signal Processing Program List	101
F.2	The Size and Numbers of Air Bubbles Processing Program List . . .	101
G	FFT Program List	102

List of Tables

4.1	Test results	60
4.2	Field Test Data	62
4.3	Laboratory tests results (1) with improved probe head	64
4.4	Laboratory tests results (2) with improved probe head	64
4.5	Laboratory tests results (3) with improved probe head	65
4.6	Laboratory tests results (4) with improved probe head	65
4.7	Air bubble size groups	68
4.8	Experiment data for air bubble size analysis (1)	69
4.9	Experiment data for air bubble size analysis (2)	69
4.10	Experiment data for air bubble size analysis (3)	70
4.11	Experiment data for air bubble size analysis (4)	70
4.12	Air bubble number and size for test sample one	71
4.13	Air bubble number and size for test sample two	71
A.1	Maximum Ratings of TOLD-9200 ($T_c = 25^\circ \text{ C}$)	88
A.2	Optical-Electrical Characteristics of TOLD-9200 ($T_c = 25^\circ \text{ C}$)	89
B.1	Circuit Device list	92
D.1	Electro-Optical Characteristics	97
E.1	Circuit Device List	100

List of Figures

1.1	Longitudinal section of a step index fiber optic showing guided and leaky rays	4
1.2	Temporal coherence	7
1.3	Spatial coherence	8
2.1	Reflection and refraction at the boundary separating two media with refractive indices n_1 and n_2 , respectively	11
2.2	Reflected light intensity at the tip of a multimode fiber optic sensor in fresh concrete and in an air bubble	13
2.3	System block diagram	14
2.4	Sensor preparation steps	17
2.5	Fiber optic sensor structure	18
2.6	Principle of system fiber optic sensor	19
2.7	Reflected light intensity in air, concrete and water	20
2.8	Fiber optic sensor relative response level in air and fresh concrete . .	21
2.9	Fiber optic sensor response speed	23
2.10	Block diagram of laser diode control and drive circuit	24
2.11	Zero bias, photoamperic operational circuit for photodetector	27
2.12	Block diagram of analog amplifier and the lowpass filter	28
2.13	Active lowpass filter circuit	30
2.14	Block diagram between analog amplifier and computer	33

3.1	Signal flowchart of test data	38
3.2	Test signal $X_0(n)$	41
3.3	Filtered data $X_1(n)$ recorded by channel 1 representing the baseline along the sensor path	43
3.4	Reflected light intensity variations in different locations of same con- crete	44
3.5	Signal after a digital comparator operation	45
3.6	Signal after a digital adder operation	46
3.7	FFT of test data signal	49
3.8	FFT of baseline signal	50
3.9	FFT of signal $y_1(n)$	51
3.10	FFT of signal $y_3(n)$	52
3.11	Example of one experiment test data calibration	54
3.12	Amplifier gain effect on signal range	56
3.13	Two test data using different amplifier gain in same concrete	57
4.1	Three test methods comparison	61
4.2	U-shaped sensor protection head	63
4.3	Effect of bubble size and spacing on the amplitude of reflected light signal	67
4.4	Air bubble size and numbers in concrete analysis using fiber optic method for test sample one	72
4.5	Air bubble size and numbers in concrete analysis using microscopic method for test sample one	73
4.6	Air bubble size and numbers in concrete analysis using fiber optic method for test sample two	74
4.7	Air bubble size and numbers in concrete analysis using microscopic analysis method for test sample two	75
4.8	Air bubble size and number in concrete analysis using microscopic analysis method for test sample two slice (1)	76

4.9	Air bubble size and number in concrete analysis using microscopic analysis method for test sample two slice (2)	77
4.10	Air bubble size and number in concrete analysis using microscopic analysis method for test sample two slice (3)	78
4.11	Air bubble size and number in concrete analysis using microscopic analysis method for test sample two slice (4)	79
4.12	Air bubble size and number in concrete analysis using microscopic analysis method for test sample two slice (5)	80
4.13	Air bubble size and number in concrete analysis using microscopic analysis method for test sample two slice (6)	81
4.14	Air bubble size and number in concrete analysis using microscopic analysis method for test sample two slice (7)	82
4.15	Air bubble size and number in concrete analysis using microscopic analysis method for test sample two slice (8)	83
A.1	PIN Connection of TOLD-9200	88
B.1	Laser Diode Control and Drive Circuit	91
C.1	Operation Principle of Axially Tilt Adjustable Components: For small tilt angles (θ), $z = t = f\theta$, $y = 2f\theta$, $\theta = x/L$	94
D.1	PIN Connection	96
E.1	Analog Amplifier and Filter Circuit	99

Chapter 1

Introduction

1.1 Air Content in Concrete

Quality control and condition analysis through nondestructive testing in concrete is one of the important problems in the field. In the placement of cast-in-place concrete, fresh concrete must be tested to ensure that it meets contractual specifications. Among these specifications to be tested is the entrained air percentage. The percentage of entrained air in concrete must be well controlled since the freezing and thawing durability would be impaired if the concrete contained an insufficient amount of air, and the strength would be unnecessarily reduced if the percentage of air became excessive.

There are some common methods that are used to measure entrained air percent in freshly mixed concrete:

- the pressure method
- the volumetric method

- the gravimetric method

The traditional devices used to determine entrained air percentage are: Precision air entrainment meter (pressure method) and Roll-A-Meter (volumetric method), etc. Most of which are quite cumbersome, time consuming, and of questionable accuracy. This thesis presents a methodology using fiber optic sensor technology to develop a test method and an instrument to determine the amount and distribution of entrained air in freshly mixed concrete.

1.2 Fiber Optic Sensors

Fiber optic sensor development has matured to the point where the impact of this new technology is now evident. There are many advantages in using fiber optic sensors [1].

- good electrical isolation
- immunity to electro-magnetic interference
- safety in explosive environments
- low signal attenuation
- compactness
- flexibility

Furthermore, fiber optic sensor exhibits high sensitivity and wide dynamic range and are suitable for noncontact operations. It has fast response and can be miniaturized and ruggedized [2].

The ray optical representation of a fiber optic waveguide is shown in Figure 1.1. A dielectric rod of refractive index n_1 is enclosed in a dielectric tube of lower refractive index n_2 . A ray of light propagating along the rod will be totally internally reflected at the interface if

$$\sin\theta > \frac{n_2}{n_1} \quad (1.1)$$

due to applying Snell's law [3] at the interface. If this inequality is not met, then light will leak from the core of the fiber to the cladding, and will be radiated. In the case of a fiber optic guide, the central region is referred to as the fiber core and the surrounding tube as the cladding. Rays propagating according to Equation 1.1 are guided rays, and the remainder are leaky rays.

Fiber optic sensors are commonly classified according to the way signals are modulated to the optical carriers. They can be classified into two categories [4]: fiber optic phase sensors and fiber optic intensity sensors. The most significant difference between a fiber optic phase sensor system and a fiber optic intensity sensor system lies in the phase and intensity responsivity of guided light in a typical fiber optic.

Ordinary photodetectors do not respond to the phase variation in an optical waveform unless an optical reference waveform is provided to establish optical interference. The stability of an optical interferometer demands spatial coherence of the optical wavefronts. Fiber optic phase sensors are often constructed of a length of a reference signal mode fiber with high sensitivity. This is to cause accumulation of the phase signal over the entire length of the fiber.

On the other hand, fiber optic intensity sensors are often made of multimode fibers with small sensors that can measure parameters at certain localized points. The optical carrier is delivered to the remotely located sensor and the return signal

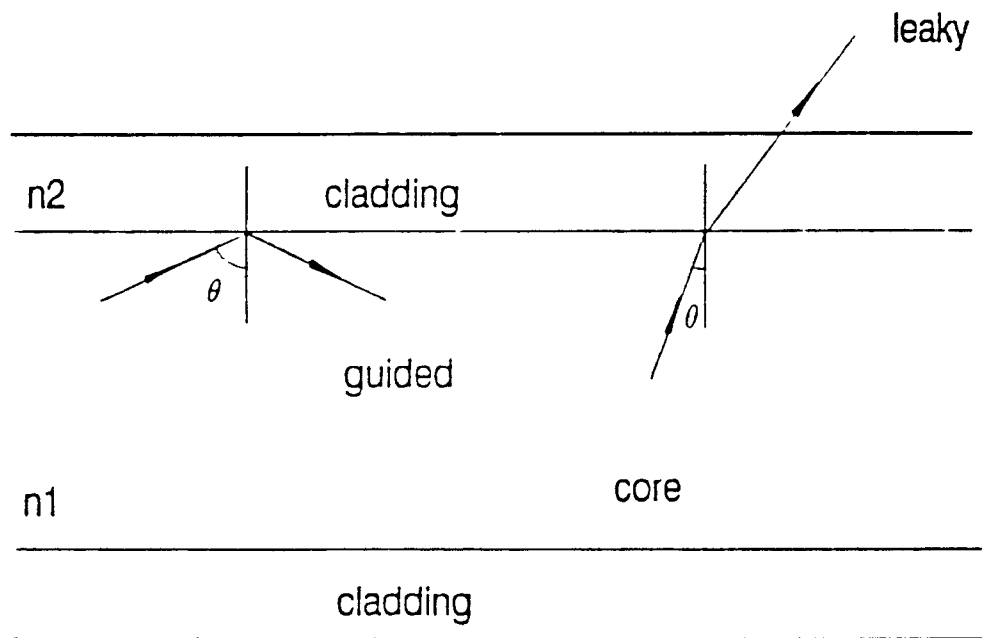


Figure 1.1: Longitudinal section of a step index fiber optic showing guided and leaky rays

is modulated in intensity by the sensor. Rather than sensitivity, the fiber optic intensity sensor tend to emphasize the electrical passiveness, electromagnetic noise immunity, ruggedness, and versatility for a very broad range of applications.

1.3 Optical Sources

Fiber optic systems employ various light sources including light emitting diodes to semiconductor laser diodes and high-power lasers. There are several advantages in using laser diodes with a fiber optic sensor among which are small size, ability to work with DC power and sufficient supply of energy for coherent light output.

Optical sources can be placed into two very broad groups: coherent and incoherent. The former category consists largely of laser devices, which exhibit a high degree of spatial coherence, that is, they are high-radiance sources, with varying degree of temporal coherence. Incoherent sources may be thought of as optical noise generators, the power output of which is the variance of the noise waveform generated.

1.4 Laser Beam Characteristics

Because of the randomness of the energy states of the electrons in most materials, there is no correlation between the individual waves of light produced by a conventional source through spontaneous emission. A conventional light source is called incoherent because it emits waves of light with no common phase relationship and with a broad range of wavelengths. A laser is a coherent source, emitting waves of light that are in phase with each other and are of nearly the same wavelength.

The general term coherence includes temporal coherence and spatial coherence [5].

Temporal coherence describes the monochromaticity of a wave and its continuity in the direction of travel. Temporal coherence depends on the spectral bandwidth of the source. The temporal coherence of a laser beam is often expressed in terms of its coherence length, which indicates the length, measured parallel to the beam, over which it can be considered a continuous wave.

Coherence length, L_c , is determined as [6],

$$L_c = \frac{c}{2\pi n \Delta f} = \frac{\lambda^2}{2\pi n \Delta \lambda} \quad (1.2)$$

Where Δf , and $\Delta \lambda$, are spectral bandwidth (in terms of frequency or wavelength), c is the speed of light in vacuum, and n is the index of refraction of the propagation medium. Laser diodes with coherence length of up to several dozen micrometers are suitable for application in interferometry.

Spatial coherence describes the continuity and uniformity of a wave in the direction perpendicular to the direction of travel. A spatially coherent beam can be focused to a much smaller spot than can the beam from an incoherent source.

1.5 Light Sensing Elements

The most widely used light sensing elements in fiber optic systems are semiconductor diodes. These photodetectors rely on the energy of the incident photon either to produce an electron-hole pair in the semiconductors or to cause the release of a primary electron from the cathode. Thus the detection process is in effect a

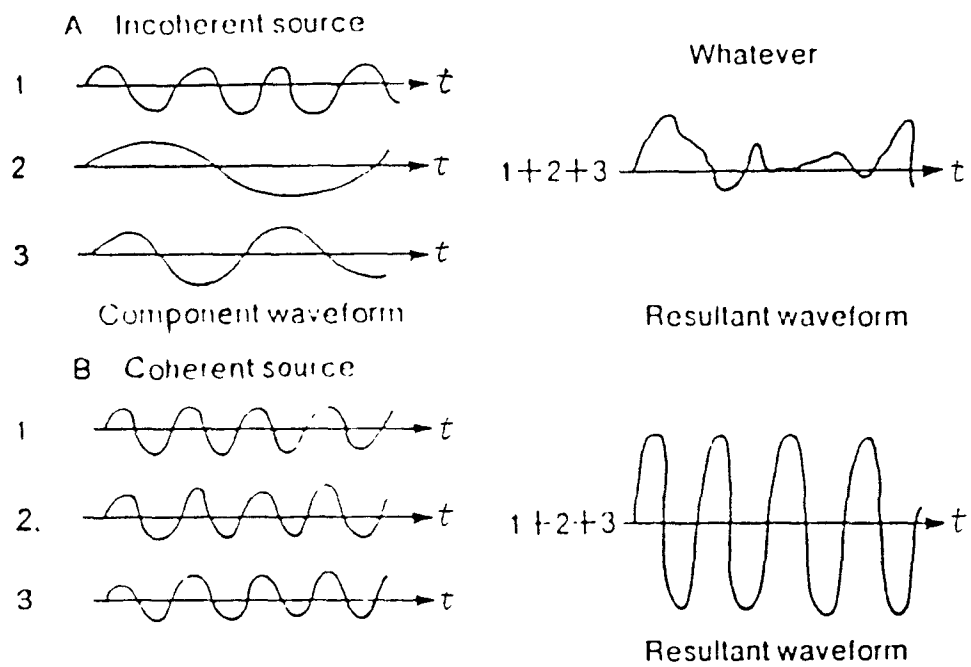
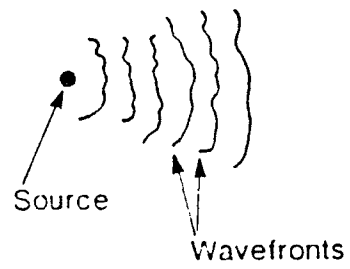


Figure 1.2: Temporal coherence

A Incoherent source



B Coherent source

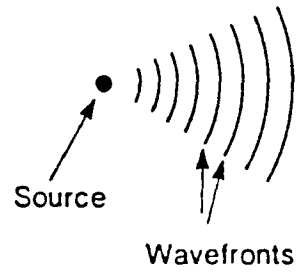


Figure 1.3: Spatial coherence

photon counting action, and as such is basically a statistical process due to the fact that counting is involved.

There are currently four principal types of semiconductor photodetector in common use in optical systems [8]: the PIN diode, the avalanche photodiode (APD), the PIN-FET hybrid module and photoconductors. The basic detection process is identical in all these devices, that is the creation of electron-hole pairs by incident photons, and so the wavelength response of the detector is determined primarily by the bandgap of the semiconductor material.

Chapter 2

System Structure and Principle

2.1 Measuring Methodology

When a ray of light is incident on a boundary separating two different media, some of the energy is reflected back into the first medium and the remainder is refracted as it enters the second medium. See Figure 2.1.

The refracted ray also lies in the plane of incidence and on the opposite side of the normal. This relationship, experimentally established by Snell, is known as Snell's law. [3]

$$\frac{\sin\theta_1}{\sin\theta_2} = \frac{n_2}{n_1} \quad (2.1)$$

where θ_1 is the angle of incidence, θ_2 is the angle of refraction. n_1 , n_2 are two different media refractive indices.

Furthermore, according to Fresnel's laws [9] of reflection , the ratio of the amplitudes of the reflected and incident waves can be approximately expressed for normal incidence as

$$\frac{R}{E} = \frac{n_2 - n_1}{n_2 + n_1} \quad (2.2)$$

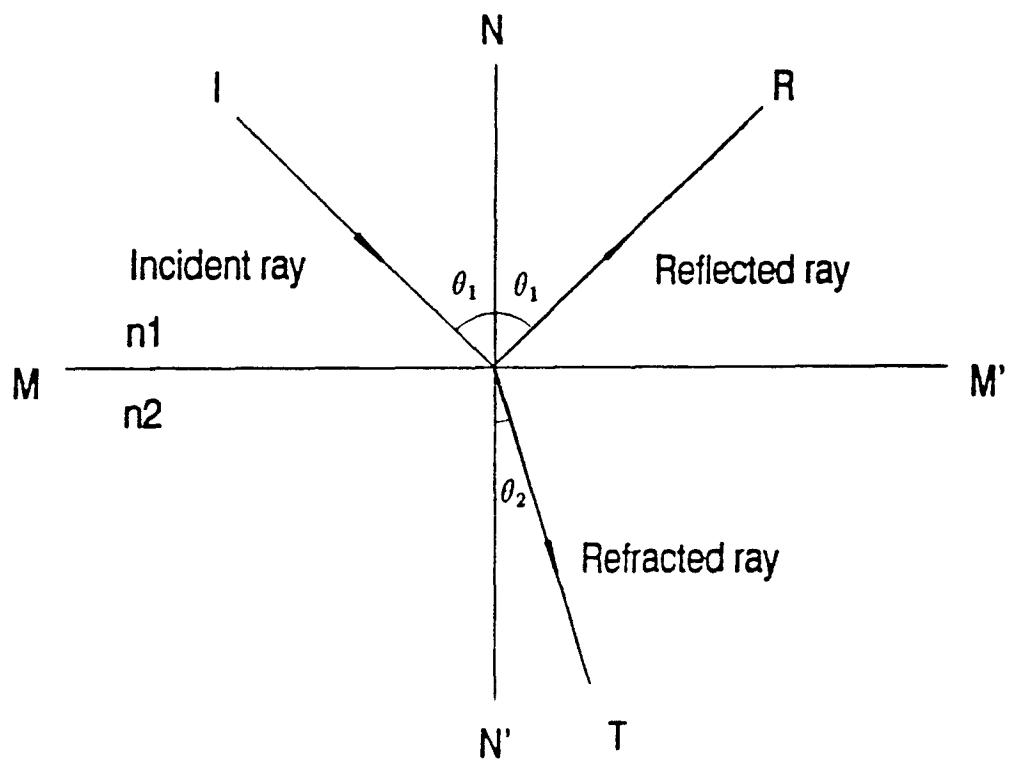


Figure 2.1: Reflection and refraction at the boundary separating two media with refractive indices n_1 and n_2 , respectively

where the symbols E and R are amplitudes of the electric vectors in the incident and reflected light, respectively.

The intensity varies as the square of the amplitude, hence the reflection at normal incidence is

$$\frac{R^2}{E^2} = \left(\frac{n_2 - n_1}{n_2 + n_1} \right)^2 \quad (2.3)$$

The simple concept of light intensity loss as a result of differences in indices of refraction between two mediums when coupled with fiber optics will result in a powerful measurement instrument.

As shown in Figure 2.2, if the light exiting end of an optical fiber ($N \doteq 1.44$) meets an air bubble ($N=1.0003$), most of the light will reflect back due to the large difference between the indices in these mediums. On the other hand, the same fiber tip, when immersed in fresh concrete, exhibits a large decrease in the intensity of the reflected light. The glass-air interface at which total internal reflection occurred is eliminated and the index of the glass is nearly matched by the concrete. When this happens, the light is no longer totally internally reflected and most of the optical power is transmitted from the fiber end into the concrete.

2.2 System Structure and Basic Components

The block diagram in Figure 2.3 describes the components of the the fiber optic sensor system.

A diode laser emitting visible light at 670 nm wavelength is employed in transmitting optical signals. A silica glass multimode optical fiber delivers the light to a

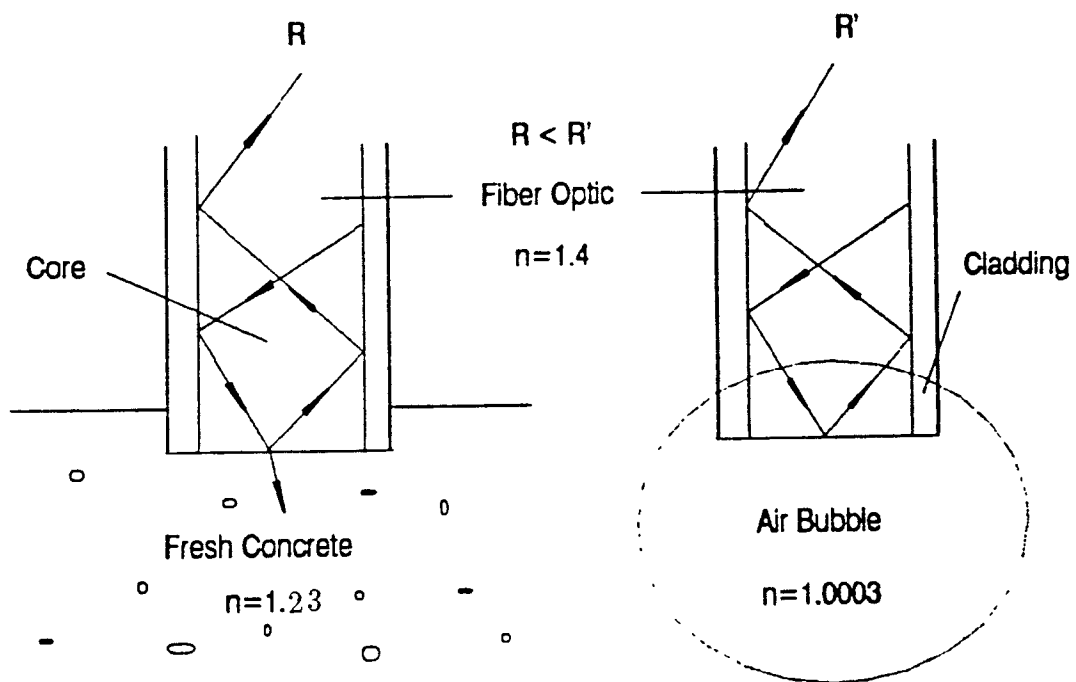


Figure 2.2: Reflected light intensity at the tip of a multimode fiber optic sensor in fresh concrete and in an air bubble

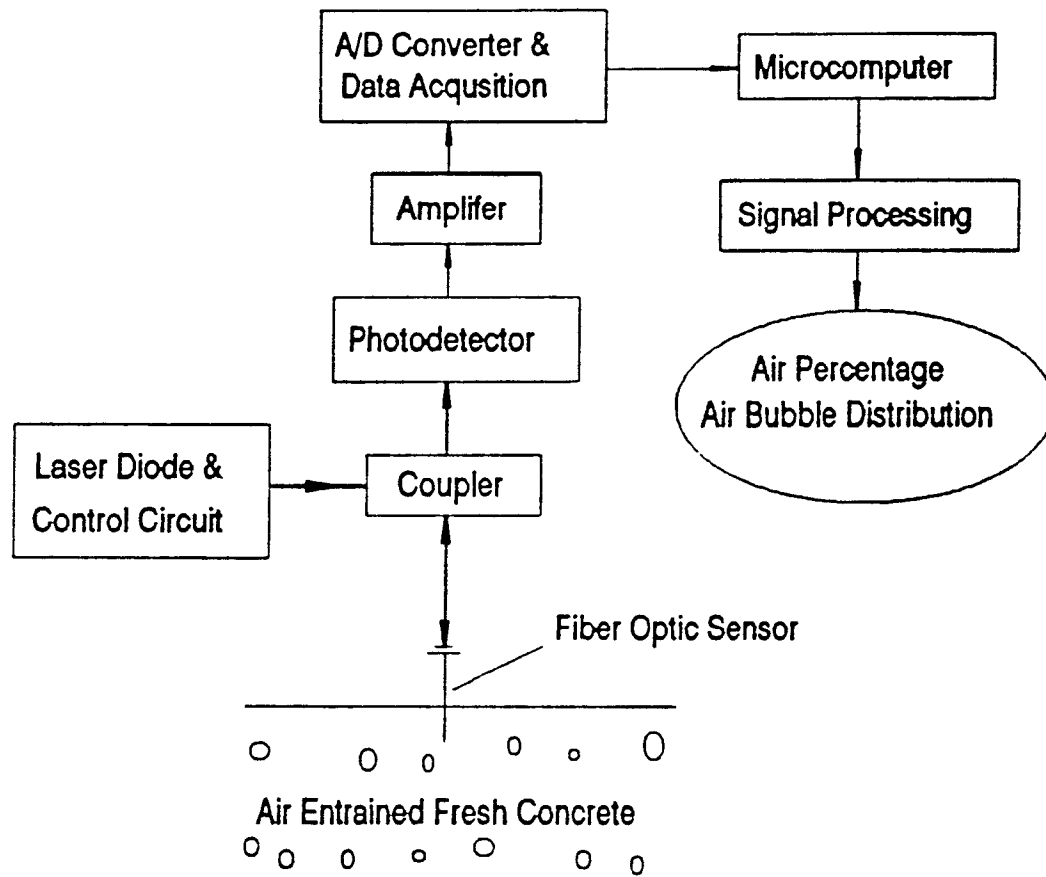


Figure 2.3: System block diagram

coupler; the coupler then directs the signal to the exit end of the fiber. Depending on the amount and number of air bubbles in the fresh concrete, light will reflect back into the fiber. The coupler separates the reflected and incident signals, and directs the reflected signal to a photodetector. Reflected light intensity signal is changed to an electrical current in the photodetector and amplified through an amplifier. At this stage, the voltage output of the amplifier is converted to a digital signal via an analog-to-digital converter. Real-time data is then transferred to a laptop computer for data processing.

2.3 System Fiber Optic Sensor Structure and Principle

The fiber optic sensor used in this system belongs to the fiber optic intensity sensor category. A multimode fiber optic cable (core/cladding, $50/125\mu\text{m}$) is used to prepare the sensor. The preparation of the sensor involved extreme care. The following steps illustrate the preparation procedure: (1) Commercially available “Connector Termination Kit” manufactured by the Newport Corporation was used in this study. One side of the cable is linked with a multimode SMA fiber connector according to the procedures described in the manufacturers brochure [10]. The following preparation steps are depicted in Figure 2.4. (2) Enlarge the hole in the SMA connector to accommodate a metallic syringe needle tube. (3) Put the metallic syringe needle through the enlarged opening of the SMA connector, and hold in position as shown. (4) Decide on proper length of fiber optic, strip the cable, and pass it through the syringe needle as shown. (5) Apply regular epoxy inside the SMA housing, and slightly pull the fiber optic back and forth, so that the fiber outer walls carry some epoxy into the syringe needle tube. (6) Proceed with normal

SMA connection procedure of cable to SMA connector as in Step (1). (7) Wait twenty-four hours for the epoxied connection to dry. (8) The tip of the needle is then polished to a tapering end using lapping sheets. (9) The tip of the needle is then polished in an angle of 90° . The structure of the sensor is shown in Figure 2.5. The main purpose of using a needle shaped sensor head was to get a good response (not stick with cement) and to protect the sensor tip.

In this sensor, the guided light, emitted by a laser diode, is reflected at a fiber optic sensor tip (interface) after being modulated by the varying refractive indices of air, concrete and water. A light intensity portion is reflected back, depending on the medium (air, concrete or water) present at the fiber tip and is detected by a photodetector after separation from emitted light in the coupler as shown in Figure 2.6. This design uses only one fiber optic for bidirectional light transmission [11]. Figure 2.7 shows different analog output voltage values that represent reflected light intensity in air, concrete and water. It shows that this sensor can detect the index difference between different mediums. In general, two parameters define sensor performance: (1) Relative response level in air and fresh concrete. (2) Response time. Acceptable relative response level in air and fresh concrete according to experiments should be larger than 0.7 volts. Figure 2.8 shows the relative response level in air and concrete measured by two different sensors; the large and small relative response levels are compared. In this system, fiber optic sensor response is defined as the response time from the reflected light intensity value of water to the stable reflected light intensity value of air. From experience it has been found that a good fiber optic sensor should have a response time of less than 0.2 seconds. Figure 2.9 shows the response of a fast and a slow sensor. Slow sensors are not so sensitive, and therefore, they will not be able to detect all the phenomena effectively. In the

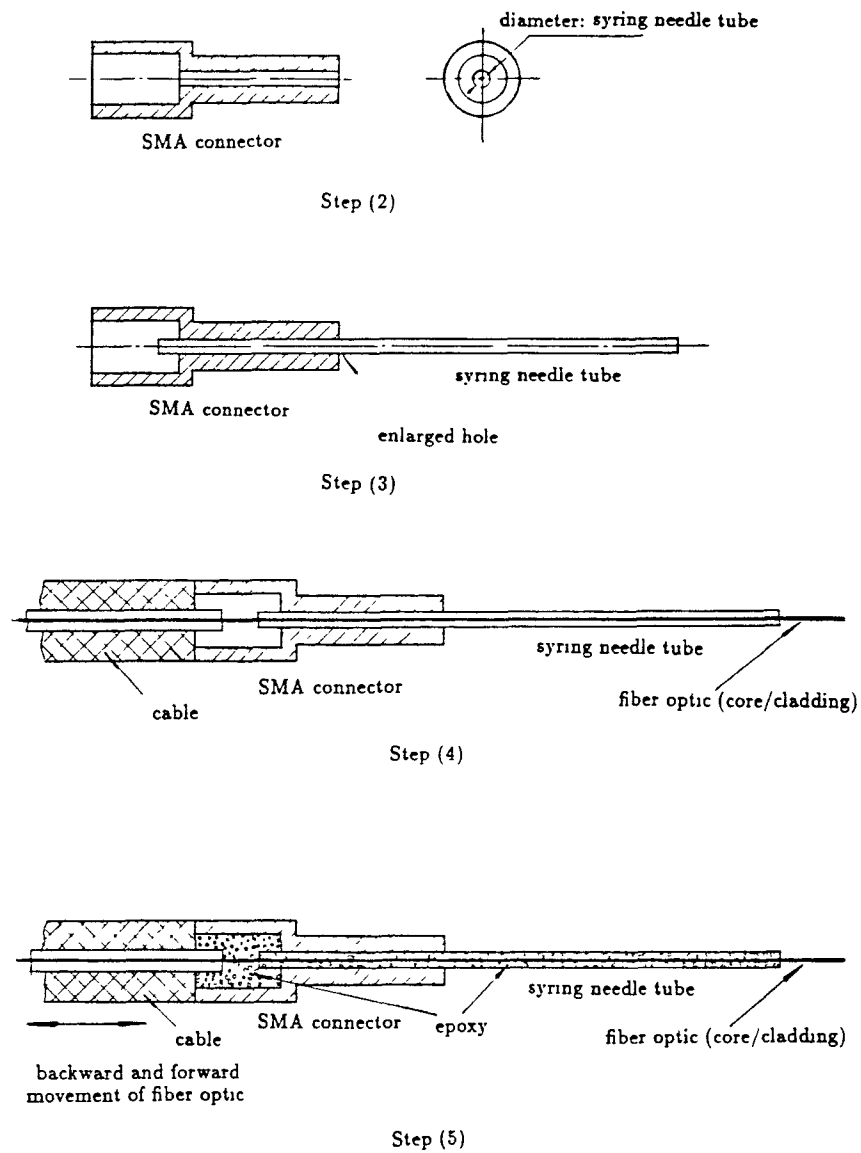


Figure 2.4: Sensor preparation steps

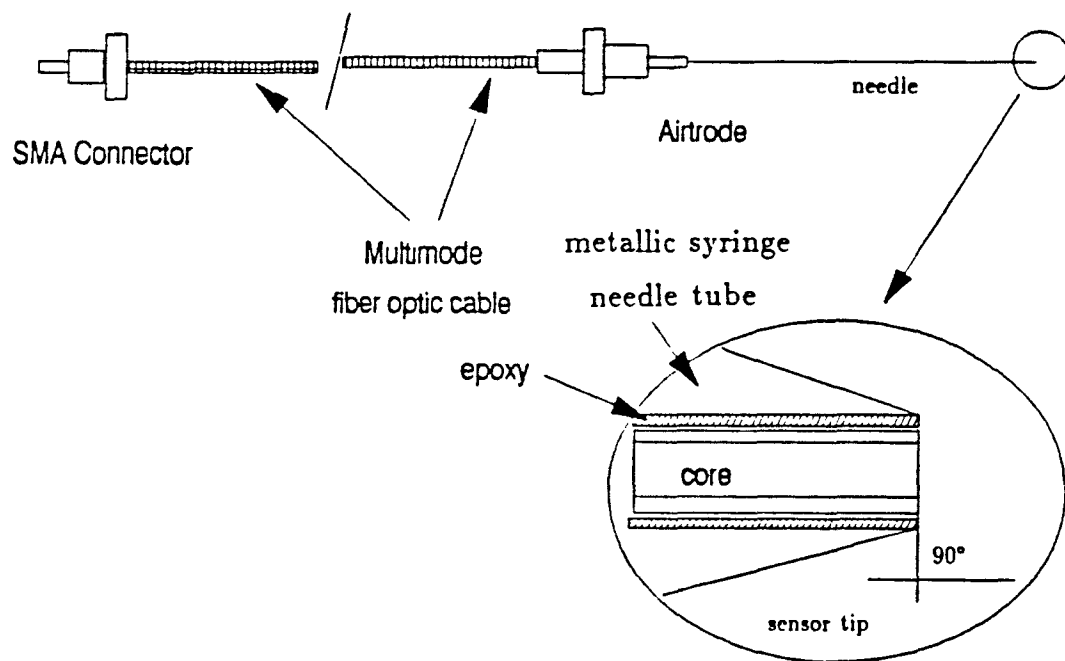


Figure 2.5: Fiber optic sensor structure

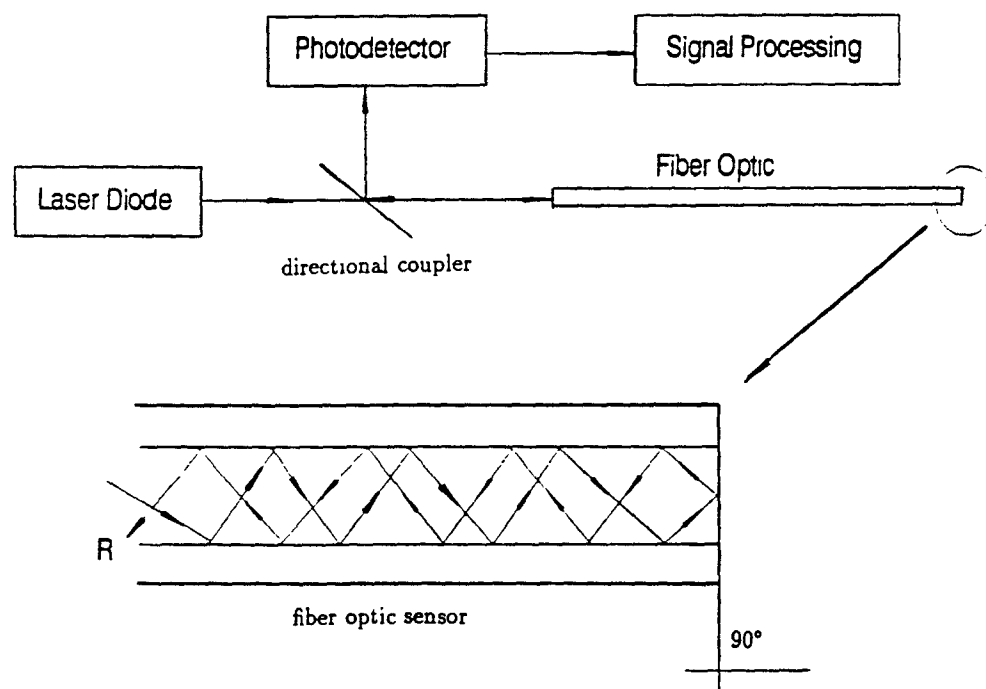


Figure 2.6: Principle of system fiber optic sensor

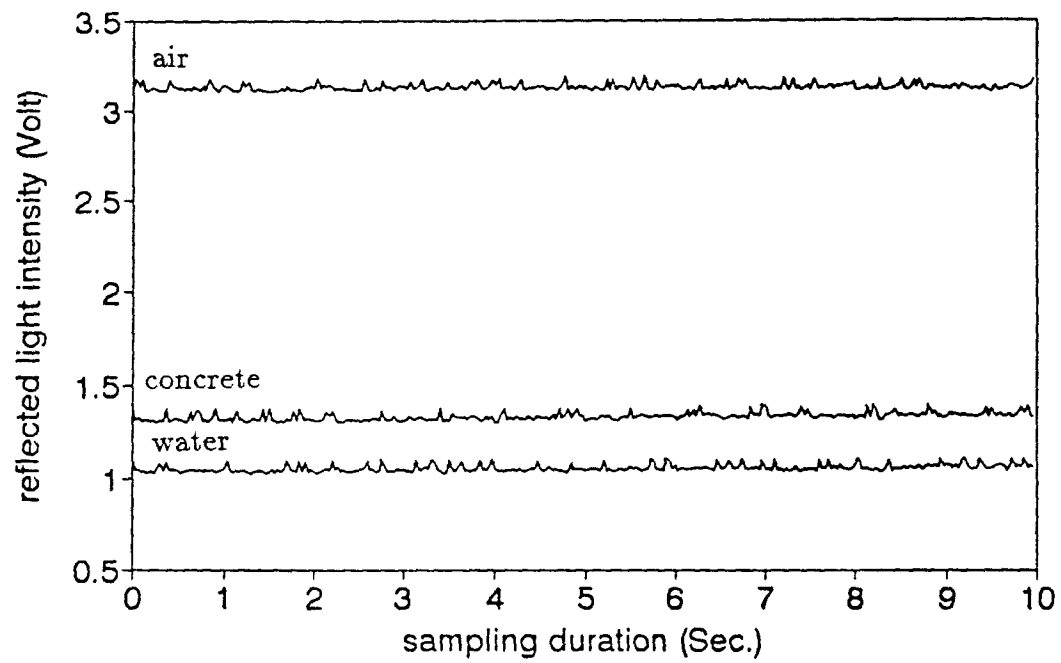


Figure 2.7: Reflected light intensity in air, concrete and water

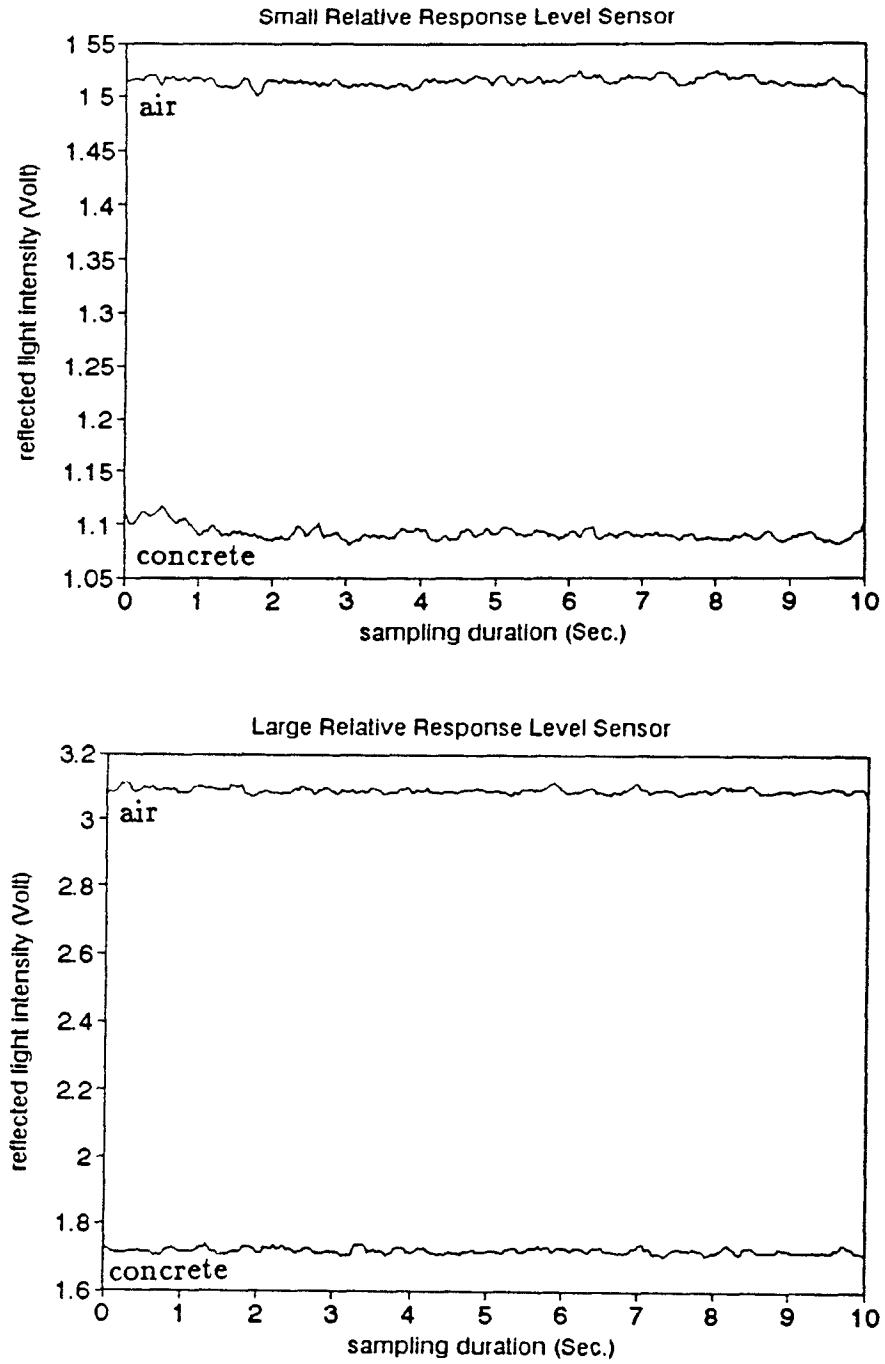


Figure 2.8: Fiber optic sensor relative response level in air and fresh concrete

present studies, it was found that, the sensor speed depends on the probe heads polishing procedure step (8) and (9) as explained earlier. In Figure 2.9, slope of the fast sensor is 13.4 volts/sec.

2.4 Laser Diode

In this system, a visible laser diode (wavelength: 670 nm) TOLD-9200 manufactured by TOSHIBA is used as a system optical source. The description of the structure of TOLD-9200 is provided in [13]. The technical data of TOLD-9200 is shown in Appendix A.

2.5 Laser Diode Control and Drive Circuit

The power output of a laser diode is easily changed by the fluctuation in the ambient temperature. A drive circuit with an automatic power control (APC) function, acting as a feedback loop from the output of the monitor photodiode to the input of the laser diode, is normally used to maintain constant power output in an environment where temperature may vary.

A drive circuit with APC function has also been used in the present system. Figure 2.10 shows the block diagram of laser diode control and drive circuit with APC function. The circuit details and device list have been shown in Appendix B.

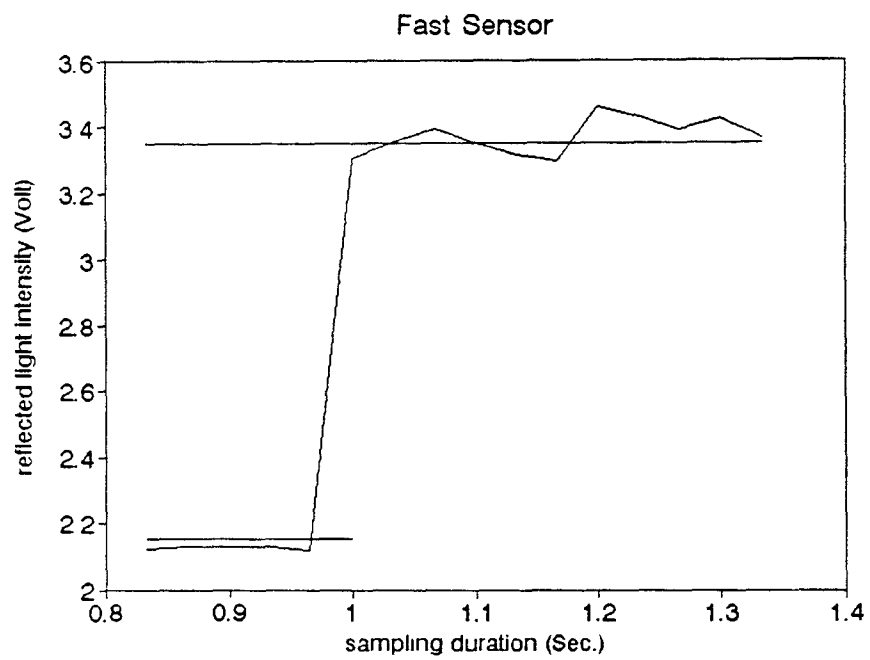
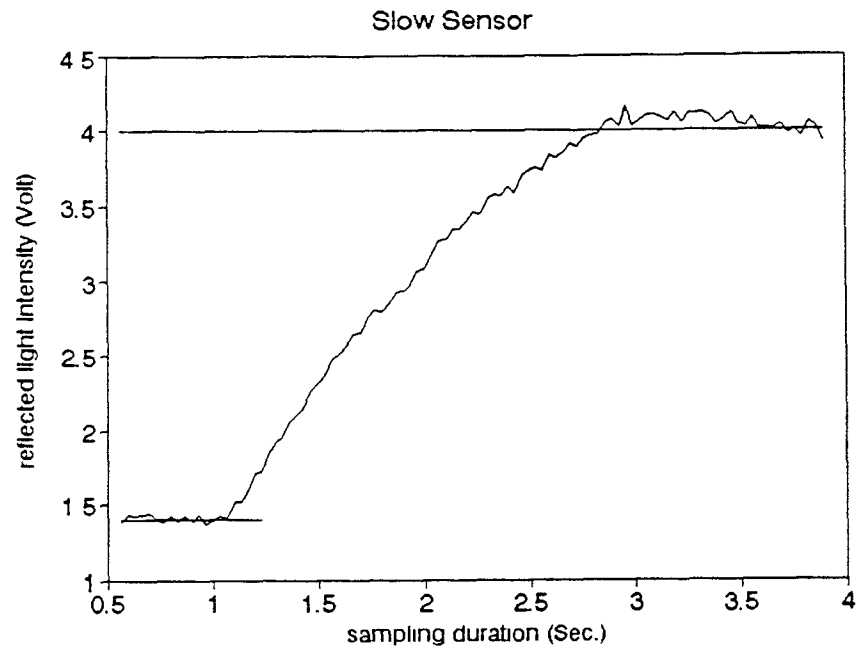


Figure 2.9: Fiber optic sensor response speed

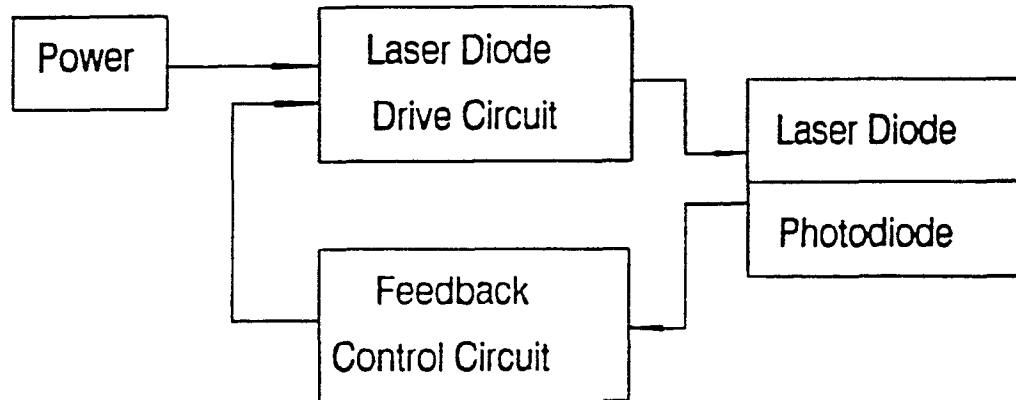


Figure 2.10: Block diagram of laser diode control and drive circuit

2.6 Laser to Fiber Source Coupler

The laser source coupler is used to overcome the problem of precision alignment while maintaining low losses in the intensity output. In this system, a multimode laser to fiber source coupler manufactured by OZ Optics Ltd. is used. This source coupler utilizes the properties of lenses in combination with a novel tilt method to achieve submicron resolution. This method is based on precision control of the angle between the laser beam and receiver. Operation principle is shown in Appendix C.

2.7 Multimode Fiber Directional Couplers

The directional coupler used in this system is multimode three-port PC3-C-50 coupler manufactured by CANSTAR. It provides a high directivity (-25 dB), low loss beam splitting for fiber system operating at 400 to 1600 nano-meter, and a convenient beam splitting with negligible temperature and polarization dependence. The beam splitting ratio is 50 percent. It serves as alignment-free beamsplitters, power combiners and energy taps.

2.8 Photodetector and Operational Circuit

In the present study, an AX65-R2F photodiode manufactured by Centronic Inc. is employed as the light sensing element. The AX65-R2F is a silicon photodiode specially designed for fiber optic applications operating in the 400 to 1000 nano-meter range. Frequency response up to 100 MHZ can be obtained when used with maximum reverse bias voltage. Its electro-optical characteristics are shown in

Appendix D.

In this system, zero bias photoamperic operation is used as the system photodetector operational circuit. For zero bias photoamperic operation, because the generated photocurrent flows through load resistance which is fixed. The resultant voltage is therefore linearly dependent on the incident radiation level. One way of achieving sufficiently low load resistance, but with an amplified output voltage is by feeding the photocurrent to an operational amplifier virtual ground as shown in Figure 2.11. The zero bias, photoamperic operational circuit for photodetector is a part of the amplifier circuit shown in Appendix E in detail. This circuit has a linear response and low noise due to the almost complete elimination of leakage current.

2.9 Analog Amplifier and Filter

An instrument amplifier usually is the first electronic device encountered in a signal acquisition, because most of the signals before amplification are very small. In this system, the reflected light intensity before amplification ranges from 0 to 7 millivolts. Therefore the present amplifier used in this system should have enough gain, sufficient linearity and low noise to fulfill the amplifier task.

A normal operational amplifier UA741CP is used to build the system analog amplifier and the filter circuit. Block diagram of the analog amplifier and the filter circuit is shown in Figure 2.12. The circuit details and components list are shown in Appendix E.

Two stages of amplification have been employed, namely, First and Second Step Amplifier. Gain is increased in two steps. After zero bias photoamperic operation,

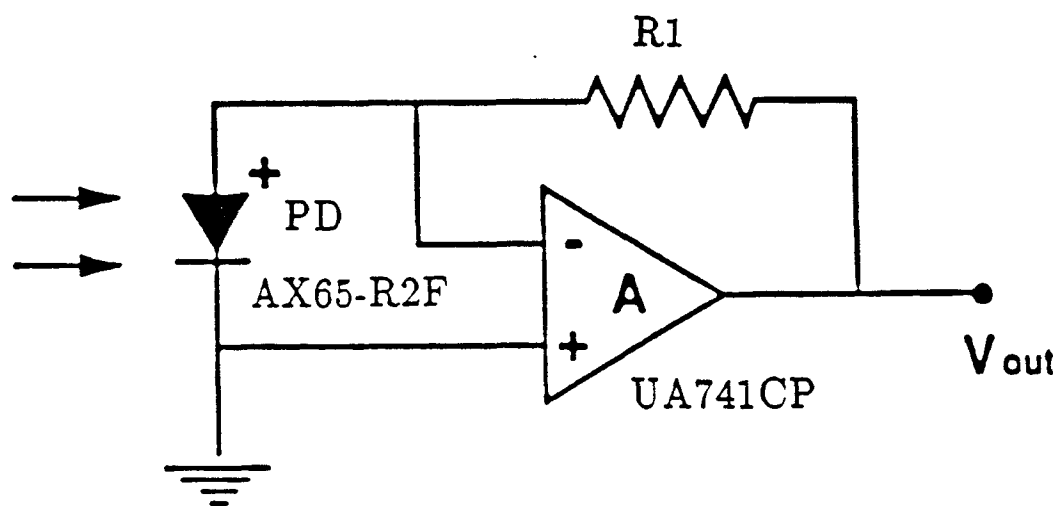


Figure 2.11: Zero bias, photoamperic operational circuit for photodetector

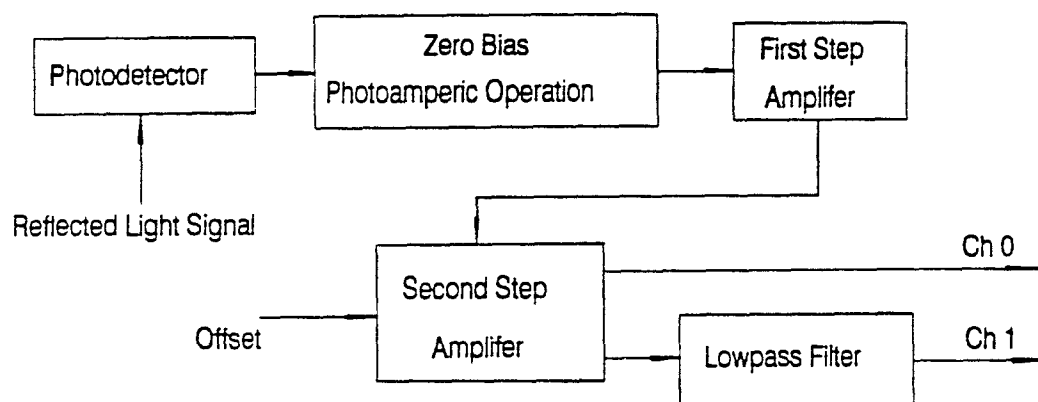


Figure 2.12: Block diagram of analog amplifier and the lowpass filter

the reflected light intensity output ranges between 0 to 7 millivolts. The gain of first stage amplifier is set between 50 to 70. Adjustments to the laser-to-fiber coupler bring about reflected light intensity changes (refer to the section of laser to fiber source coupler). The first stage gain provides flexibility in light intensity adjustments by being able to vary within the above-mentioned range. The second stage gain is fixed (Gain=10). Therefore, the gain in the amplifier varies from 500 to 700. In the second step amplifier, one offset (RV2) is added for changing the maximum signal output range within the accepted maximum input range of the data acquisition interface board ($\pm 5\text{v}$). The offset range added to the second step amplifier varies from -3.6 to +3.6 volts. If the system sensor is changed, the reflected light intensity output would change depending on the sensor tip characteristics and the sensor to directional coupler connection. The offset adjustment can bring the reflected light intensity output of the analog amplifier within the linear range.

A lowpass filter is employed in obtaining a baseline for the test signal. One portion of the signal after all the amplification stages is passed through the lowpass filter. Lowpass filters are frequently required to bandlimit measurement signals in instrumentation applications to achieve a frequency-selective function of interest. An arbitrary signal passed through a lowpass filter can result in a significant attenuation of higher frequency components, thereby defining a stopband whose boundary is influenced by the choice of filter cutoff frequency, with the unattenuated frequency components defining the filter passband. Operational amplifiers together with resistance capacitance networks are used extensively in the implementation of various types of filter network. Filters of this type are called active filters. The active lowpass filter circuit shown in Figure 2.13 is used in this system.

The filter action starts at the input V_{in} in Figure 2.13, where the incoming

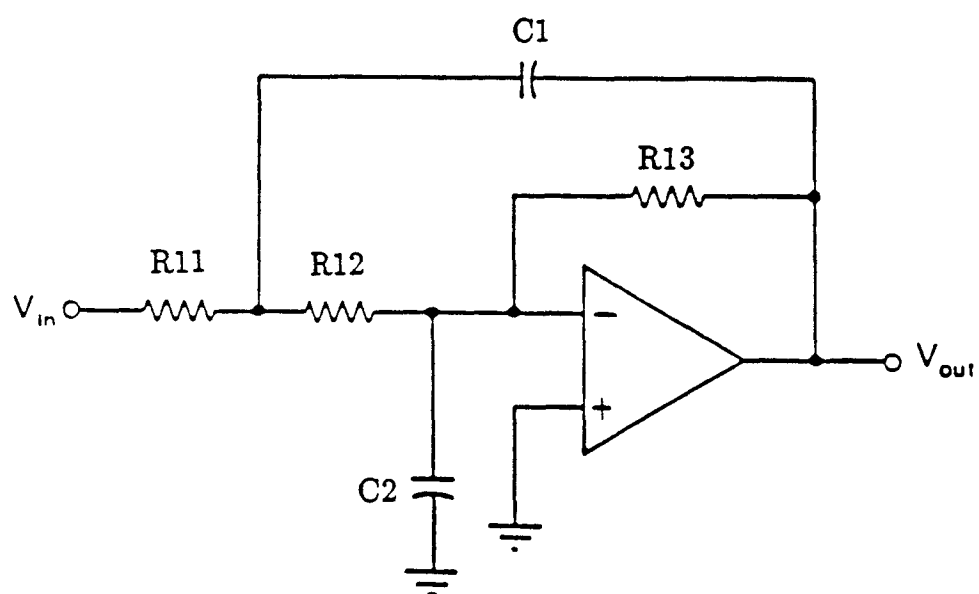


Figure 2.13: Active lowpass filter circuit

signal flows through a passive RC lowpass filter section and then into the operational amplifier. With C_1 present in the feedback loop, additional lowpass filter action takes place. In other words, C_1 has decreasing reaction at higher frequencies, resulting in more negative feedback at higher frequencies. Therefore, the operational amplifier develops higher gain at lower frequencies. The result of these combined lowpass filter actions is to produce a sharper cutoff characteristic than is provided by the passive RC filter alone.

Cutoff frequency of the filter circuit shown in Figure 2.13 is calculated by [12]:

$$F_c \approx \frac{1}{2\pi\sqrt{R_{11}R_{12}C_1C_2}} \quad (2.4)$$

where F_c is the frequency in HZ, R_{11}, R_{12} are resistance in ohms and C_1, C_2 are capacitances in farads. For example, let $R_{11} = 100k\Omega$, $R_{12} = 100k\Omega$, $R_{13} = 200k\Omega$, $C_1 = 20\mu f$, $C_2 = 4.7\mu f$. Then $F_c \approx 0.16Hz$.

By trial and error, a cutoff frequency of 0.16 HZ was chosen for the present system (after several trials of using different cutoff frequency 0.5 Hz, 0.4 Hz, 0.2 Hz etc.). The lowpass filter smooths the output signal. The lowpassed signal is used as the baseline for signal analysis. Justification for choosing a baseline as such will be given in chapter three.

2.10 Data Acquisition System and Microcomputer

A data acquisition board with an analog to digital converter is employed for transfer and storage of data in a laptop microcomputer. DAS-8 manufactured by MetraByte is an 8 channel and 12 bit high speed A/D converter and time/counter board for IBM compatible computers. The full scale input of each channel is +5

volts with a resolution of 0.00244 volts. A/D conversion time is typically 25 microseconds resulting in data throughput rates in excess of 30 Hz. The description of the structure and the programming details of this board are shown in [14]. The outputs of the analog amplifier and filter circuit are connected to the input of data acquisition board Channel 0 and Channel 1 respectively. So two separate channels of data are recorded simultaneously when the system is in operation.

T1200 manufactured by TOSHIBA is a portable personal laptop computer. It has following features [15]:

- Microprocessor: An 80C86-1 microprocessor operates an IBM PC/XT compatible BIOS ROM at 9.54 MHz
- Memory: 640 k RAM
- Keyboard: 82-key keyboard
- Disk storage: one 3.5" 20 MB hard disk drive and one DS, DD 3.5" 720 KB diskette drive
- LCD screen: A high resolution 80×25 line LCD display
- RS232-C port: An RS232-C serial port enables you connect serial device to the computer
- Operating system: MS-DOS Version 3.30
- Battery: A removable NiCad battery pack powers the computer for up to 2 hours

The block diagram of the data acquisition process is shown in Figure 2.14. In

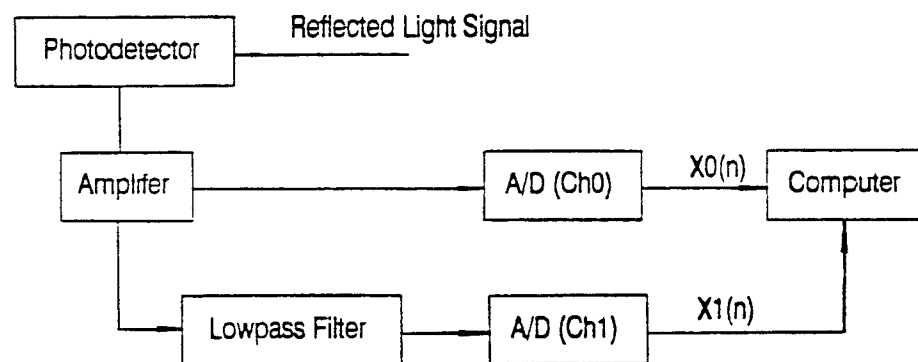


Figure 2.14: Block diagram between analog amplifier and computer

this block diagram, digital data are represented by $X0(n)$, $X1(n)$. Where n is the data point number and $X0$ and $X1$ are two channels of data acquisition: channels 0 and 1. For example, $X0(30)$ is the thirtieth data acquired from channel 0.

Chapter 3

Optical Data Signal Processing

Fiber optic sensor signal processing is a multidisciplinary subject which brings together a wide range of technologies and concepts. Determination of percent air content in fresh concrete require calibration and signal processing of optical data. This chapter gives a brief discussion of using arithmetic and digital signal processing techniques to deal with the acquired optical signals.

3.1 System Operation

In this section, operational steps leading to the evaluation of percent air in concrete will be outlined. Justifications for the individual operational steps are given subsequently. All the experimental data are recorded using an eight channels data acquisition board DAS-8 and the process is controlled by LABTECH's software ACQUIRE. Several parameters are needed to be set in the LABTECH ACQUIRE setup menu. For the present sensor, the parameters are set as follows:

- (1) Number of Analog Channels: 2 (Ch0, Ch1)

(2) Sampling Rate (HZ): 30, or more

(3) Run Duration (Sec.): 10, 20, or more

Steps involved in operation of the sensor and the system are outlined as follows:

Step 1: The sensor and the computer are turned on and the data acquisition program is triggered so as to collect data. Sampling Rate and run duration are selected (these values were chosen through trial and error, they represent minimum acceptable values, other higher settings such as sampling rate of 40 or run duration of 30 will also produce satisfactory results).

Step 2: Sensor's tip is immersed in fresh concrete for ten seconds or more (according to the run duration setting) in order to initialize the system with respect to minimum intensity readings associated with concrete.

Step 3: Sensor's tip is held in the open air in order to establish the maximum intensity reading due to air.

Step 4: Once the system is initialized, the sensor's tip is plunged into the fresh concrete and moved onward in order to sense the presence of air bubbles at different locations in concrete. The computer stops data acquisition after ten seconds or more according to the run duration. Real-time plot of reflected light intensity versus time is displayed, and the intensity values are saved in a file for further processing. Operations mentioned above will be discussed in detail in the following sections.

3.1.1 Signal Flow Operations

A signal is defined as a physical quantity that varies with time, space, or any other independent variable. Once data is acquired, recorded signals from channel 0 and 1 are the discrete-time signals to be analyzed. A discrete-time signal $X(n)$ is a function of an independent variable that is an integer. In this system, the independent variable is time. $X(n)$ was obtained from sampling an analog signal $X_a(t)$, then $X(n)=X_a(nT)$, where T is the sampling period and n is the sampling point number.

The input-output description of a discrete-time system consists of a mathematical expression or a rule, which explicitly defines the relation between the input and output signals. In our case, the rule of the input and output is defined as follows:

(1) Input to the system consists of signals acquired by channel 0 and 1 comprising the experimental and baseline input signals respectively.

(2) Output from the system is the area A_p , between the two curves created by the entire test $X0(n)$ and the baseline $X1(n)$ signals.

Flowchart representation of this relationship of the input/output operation is given in Figure 3.1.

Four digital operations are involved in this flowchart:

(1) digital comparator operation $y1(n)=C[X0(n), X1(n)]$

where C means digital comparator operation. $X0(n)$, $X1(n)$ are channel 0

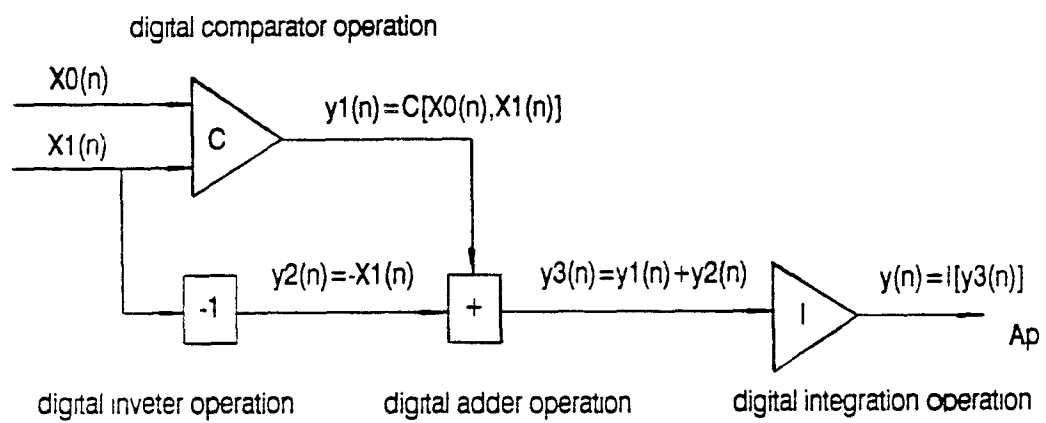


Figure 3.1: Signal flowchart of test data

test signal and channel 1 baseline signal, respectively. $y1(n)$ is the output of this operational step: number one.

Digital comparator algorithm is defined as:

$$y1(n) = \begin{cases} X0(n) & \text{if } X0(n) > X1(n) \\ X1(n) & \text{if } X0(n) < X1(n) \end{cases} \quad (3.1)$$

(2) digital inverter operation $y2(n) = -X1(n)$

where $-$ means digital inverter operation. $X1(n)$ is channel 1 baseline signal. $y2(n)$ is the output of this operational step: number two.

Digital inverter algorithm is defined as:

$$y2(n) = -X1(n) \quad (3.2)$$

(3) digital adder operation $y3(n)=y1(n)+y2(n)$

where $+$ means digital adder operation. $y1(n)$, $y2(n)$ are the output of operational step number one and two. $y3(n)$ is the output of this operational step: number three.

Digital adder algorithm is defined as:

$$y3(n) = y1(n) + y2(n) \quad (3.3)$$

(4) digital integration operation $y(n)=I[y3(n)]$

where I means digital integration operation. $y3(n)$ is the output of operational step number three. $y(n)=A_p$ is the final output.

Digital integration algorithm (Trapezoid Rule) is defined as:

$$y(n) = \sum_{i=1}^n \frac{(y3_i + y3_{i+1})(T_{i+1} - T_i)}{2} \quad (3.4)$$

where $T_{i+1} - T_i = T$, T is the sampling period. In this case, if the sampling rate is set, T is a constant number. $y3_i$, $y3_{i+1}$ are the i th and $(i+1)$ th data of $y3(n)$.

3.1.2 Signal Analysis

Figure 3.2 and 3.3 show data obtained from channels 0 and 1. Data shown in these figures were obtained by moving the sensor tip in fresh concrete for a period of ten seconds. Data shown in Figure 3.2 is recorded by channel 0 which represents the test signal $X0(n)$. It contains small and large peaks corresponding to small and large air bubbles in fresh concrete. Figure 3.3 shows the baseline signal $X1(n)$ which is the data obtained from channel 1. Baseline signal, $X1(n)$, is obtained by passing the test signal, $X0(n)$, through a lowpass filter with a cutoff frequency of 0.16 HZ as explained earlier in Chapter Two on the section corresponding to analog amplifier and filter. This signal represents the baseline for fresh concrete. Baseline describes minute variations of refractive index within concrete. The index of refraction in concrete is not constant, mainly due to it's inhomogeneity. Figure 3.4(a) shows one set of experimental data obtained by measuring the refractive index of the same

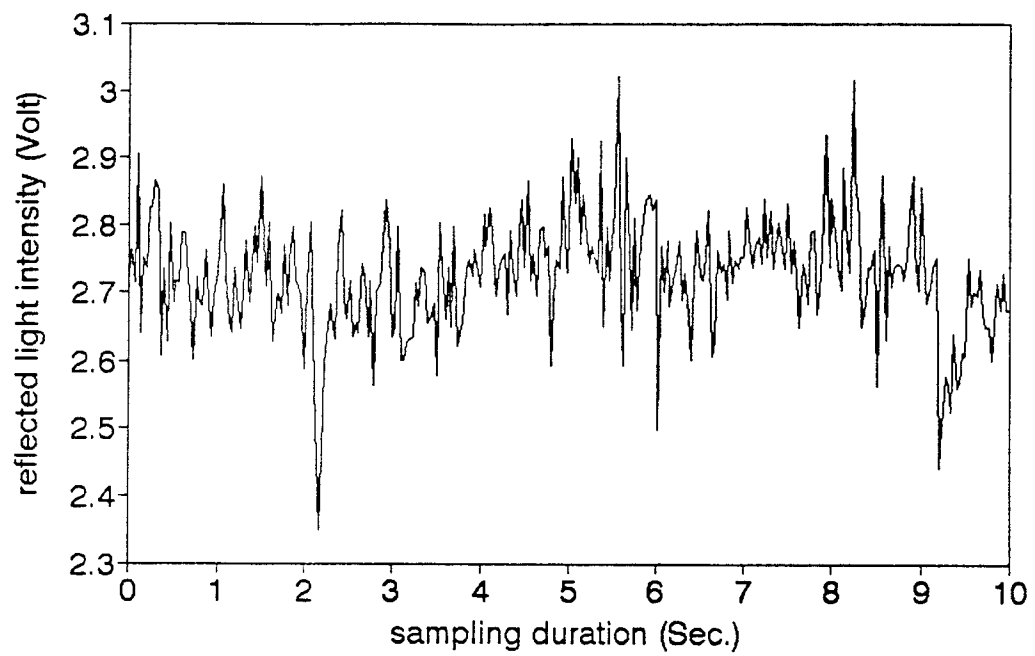


Figure 3.2: Test signal $X0(n)$

concrete at fifteen different locations. In this experiment, sensor tip is not moved and kept stationary at each test point, so only one reflected light intensity reading is recorded for every location. The regression line passing through these points (Figure 3.4(b)) represents a low frequency signal similar to the baseline shown in Figure 3.3, although they represent two different concrete specimens. The baseline amplitude is also at the concrete's level. Therefore, the baseline in Figure 3.3 represents the variation of refractive index in concrete along the sensor path.

At digital comparator stage, test signals in Figure 3.2 are compared with their baseline counterparts in Figure 3.3. Amplitude of the individual signals above the baseline represent relative measure of air bubble size distribution. Values below the baseline represent water which is not thoroughly mixed in concrete. The change in refractive index due to water brings about more refraction, and therefore lower reflected intensity. In a well mixed concrete, the number of data points below the baseline are minimal. For example, data represented in Figure 3.2 contain 24 points below the baseline, 5 points on the baseline and 271 points above the baseline. After digital comparator operation, all the values below the baseline are given the values of baseline at that point, and the remaining values are kept the same for later signal analysis (Figure 3.5). In this way, the contribution from improperly mixed water is eliminated.

Figure 3.6 represents test signal after a digital adder operation. The digital adder sums the outputs of the digital comparator and the outputs from an inverter. The output of inverter is the negative value of baseline. Therefore, in this way, signal from the comparator is subtracted from the baseline. In otherwords, Figure 3.6 depicts the net response with respect to the baseline.

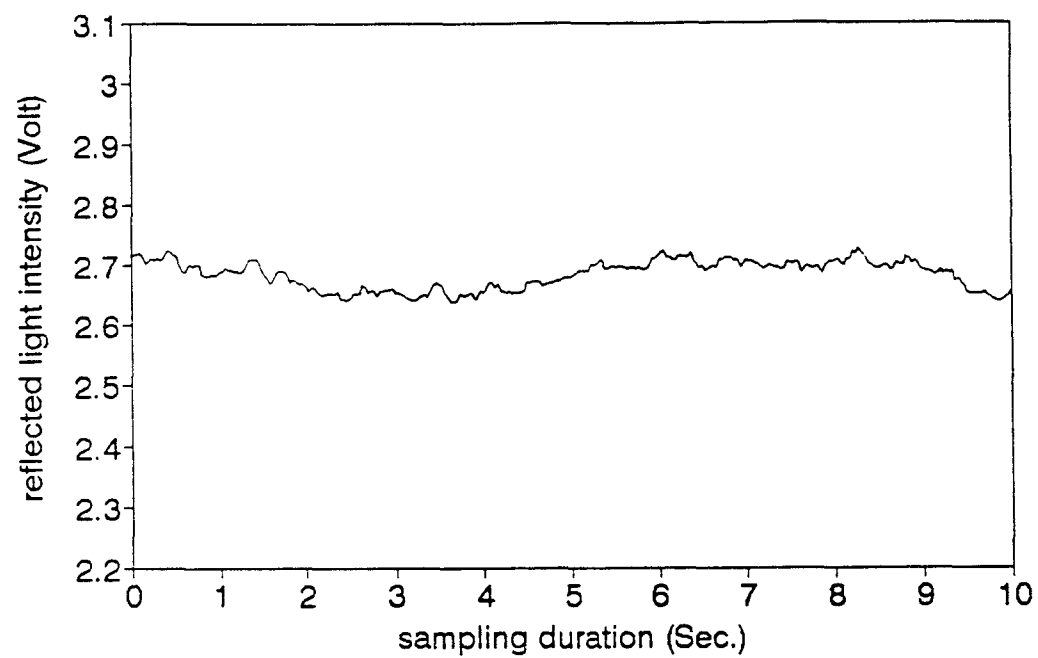
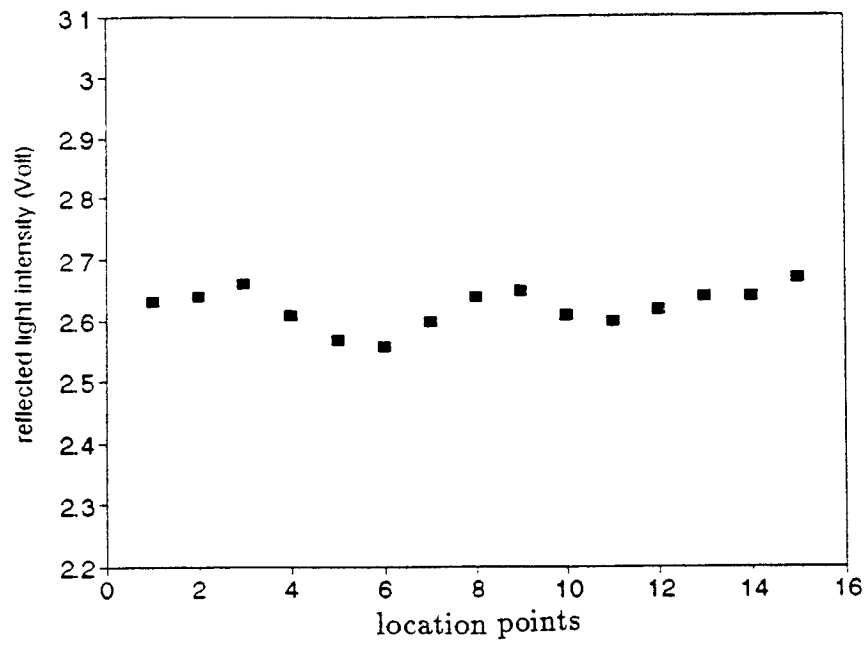
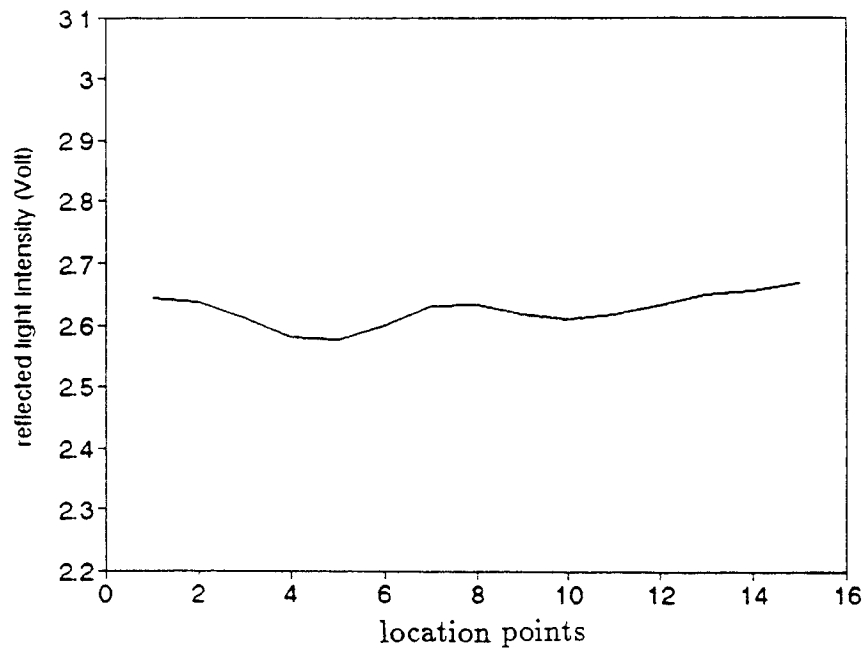


Figure 3.3: Filtered data $X1(n)$ recorded by channel 1 representing the baseline along the sensor path



(a)



(b)

Figure 3.4: Reflected light intensity variations in different locations of same concrete

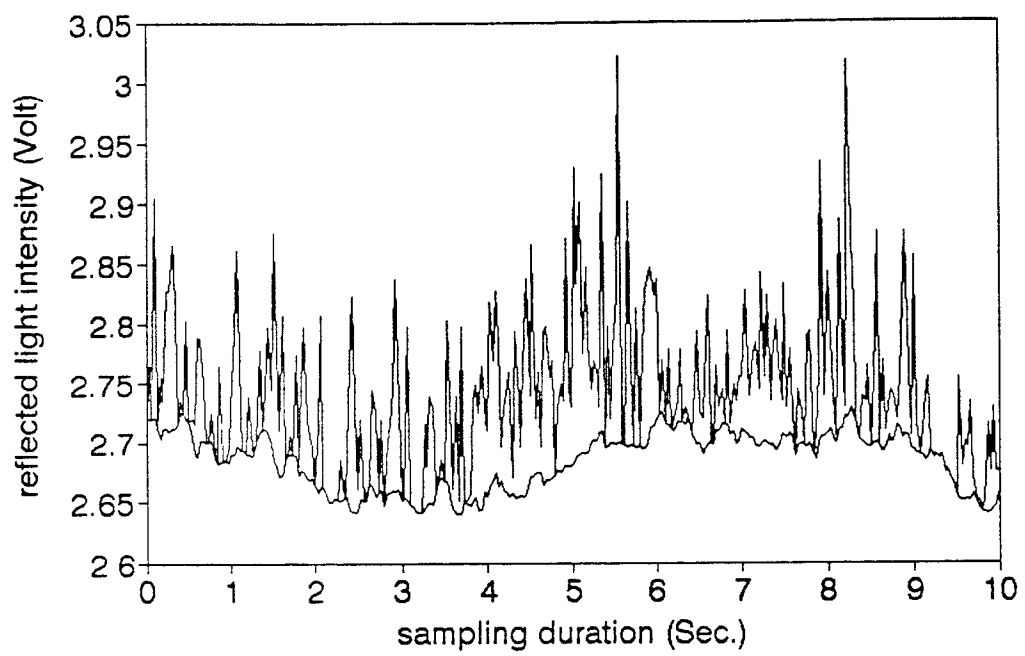


Figure 3.5: Signal after a digital comparator operation

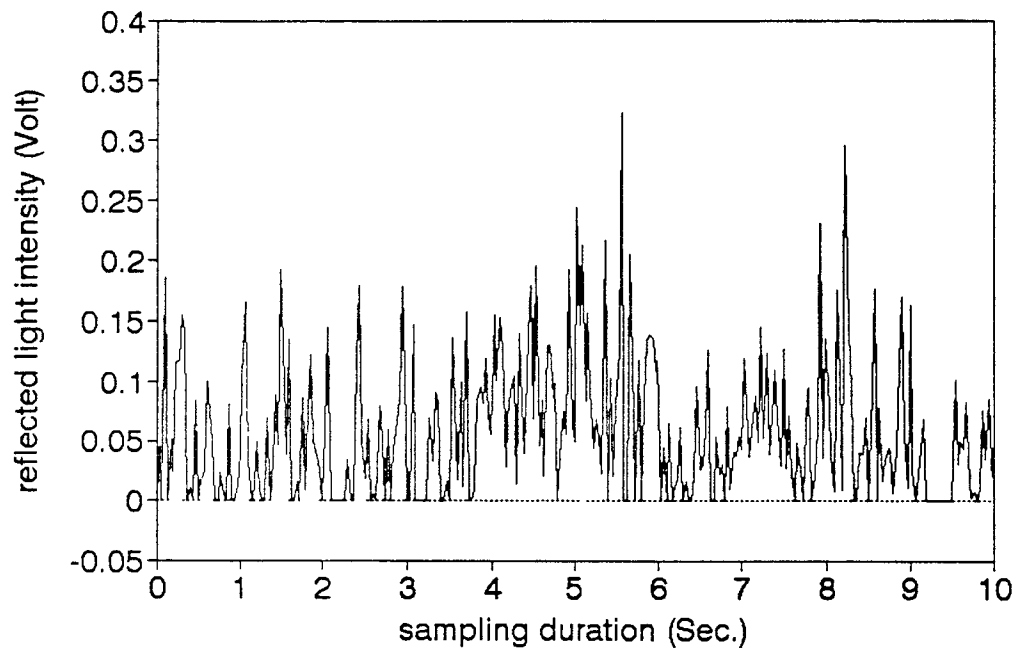


Figure 3.6: Signal after a digital adder operation

The area below the net response of the test signal in Figure 3.6 is calculated through digital integration operation. Trapezoid Integration Rule is used to perform the same. The area below the net response, A_p , together with the calibration data from the same concrete (calibration will be discussed later) will be used in the determination of air content.

3.2 Signal Frequency Analysis

Fast Fourier Transform (FFT) is playing an increasingly important role in applied engineering practices. Not only does it provide spectral analysis in speech, radar and vibration detection, but also bandwidth reduction in signal filtering. In this thesis, FFT is only used as a method to achieve frequency spectrum for every step of the signal operation and to improve these operations after analyzing frequency spectrums. Fast Fourier Transform (FFT) is simply an algorithm that can compute the discrete Fourier transform much more rapidly than other available algorithms [16]. A FORTRAN program NINFFT for computing the FFT is employed for signal frequency analysis. This program calculates the discrete Fast Fourier Transform or the inverse Discrete Fast Fourier Transform using decimation-in-frequency algorithm [17]. Program list is shown in Appendix G.

After using the program NINFFT for the data shown in the Figures 3.2, 3.3, 3.5 and 3.6, corresponding frequency spectra were obtained. They are shown in the Figures 3.7, 3.8, 3.9 and 3.10. From the frequency spectrum shown in Figure 3.7, it can be seen that the components of low frequency signal (less than 0.2 HZ) have higher spectral amplitude. This high amplitude low frequency component is made up of two parts: (1) component of the low frequency test signal, (2) component of

the signal baseline. As it is shown in Figure 3.8, the spectral amplitude of the low frequency signal is also large in the baseline, primarily because it is a lowpassed filter data. Therefore, the baseline high value of spectral amplitude in the lower frequencies has a dominant effect on the spectral response of the test signal (Figure 3.7). As it can be seen from Figure 3.10, after the digital adder operation, the baseline influence is significantly reduced as the low frequency spectral amplitudes are lowered.

3.2.1 Calibration Method

Conversion of test signal to a single value representing percentage of air requires a calibration procedure at the beginning of measurements. Step 2 and Step 3 explained in this chapter in the section corresponding to system operation provide the minimum intensity readings associated with concrete and the maximum intensity readings corresponding to air.

For the data shown in Figure 3.2, the calibration curves are shown in Figure 3.11. A more exact calibration reading in regard to minimum values associated with concrete is the curve corresponding to the baseline. In that case, there is no need to make a separate calibration reading for concrete, and the baseline reading will do the same. However, this process is computationally more costly.

The area in between the two horizontal lines, representing the response in air and concrete (Figure 3.11) correspond to 100 percent air content, A_w . In the example shown in Figure 3.11, this value is equal to 8.4 ($A_w = (3.51 - 2.67) \times 10 = 8.4$). The area under the test signal data A_p is also calculated; in the example from Figure 3.6, $A_p = 0.3385$. Percent air in concrete is then calculated as $\frac{A_p}{A_w} \times 100$. In

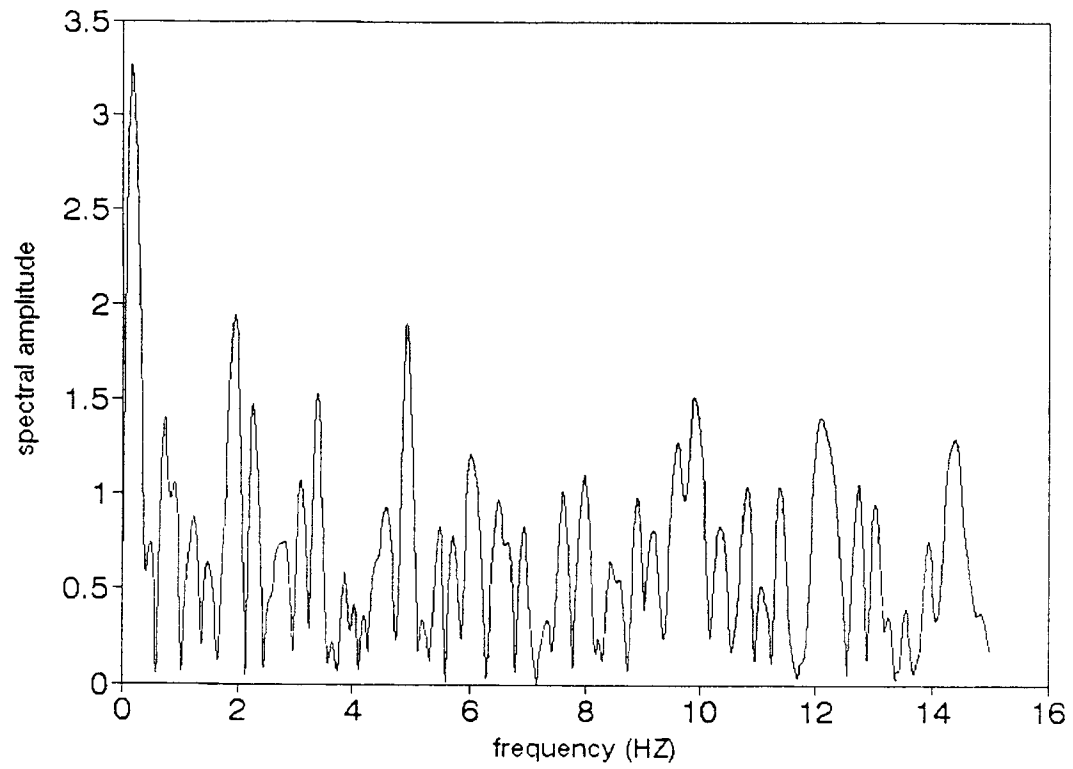


Figure 3.7: FFT of test data signal

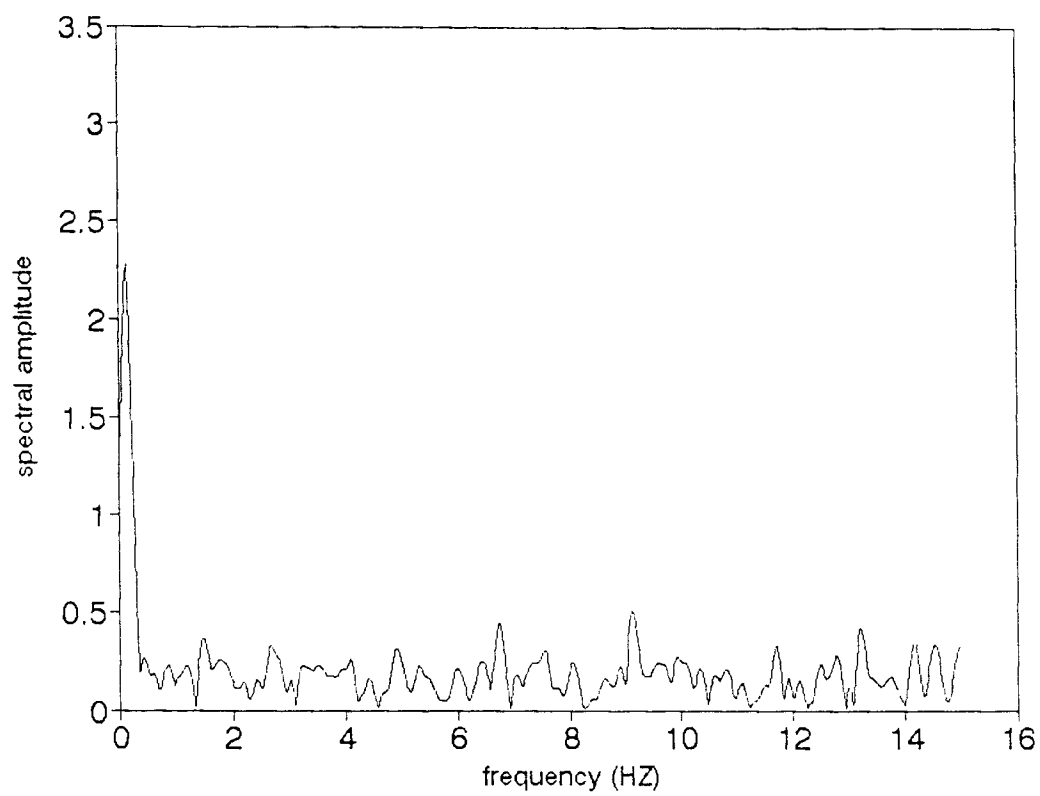


Figure 3.8: FFT of baseline signal

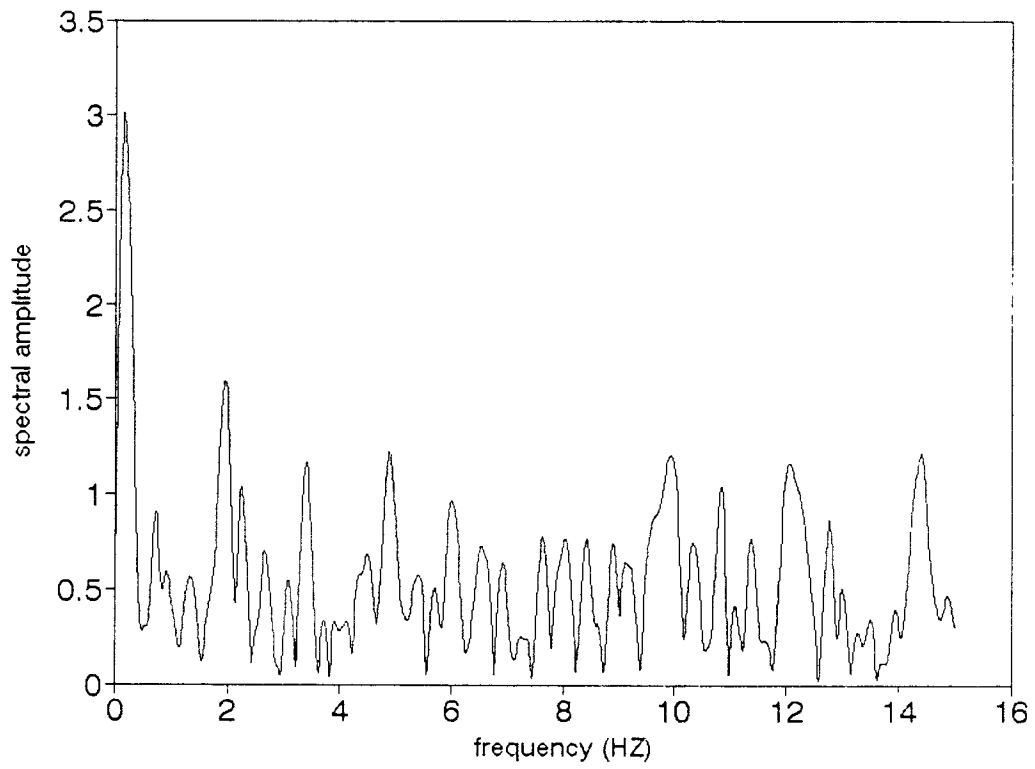


Figure 3.9: FFT of signal $y_1(n)$

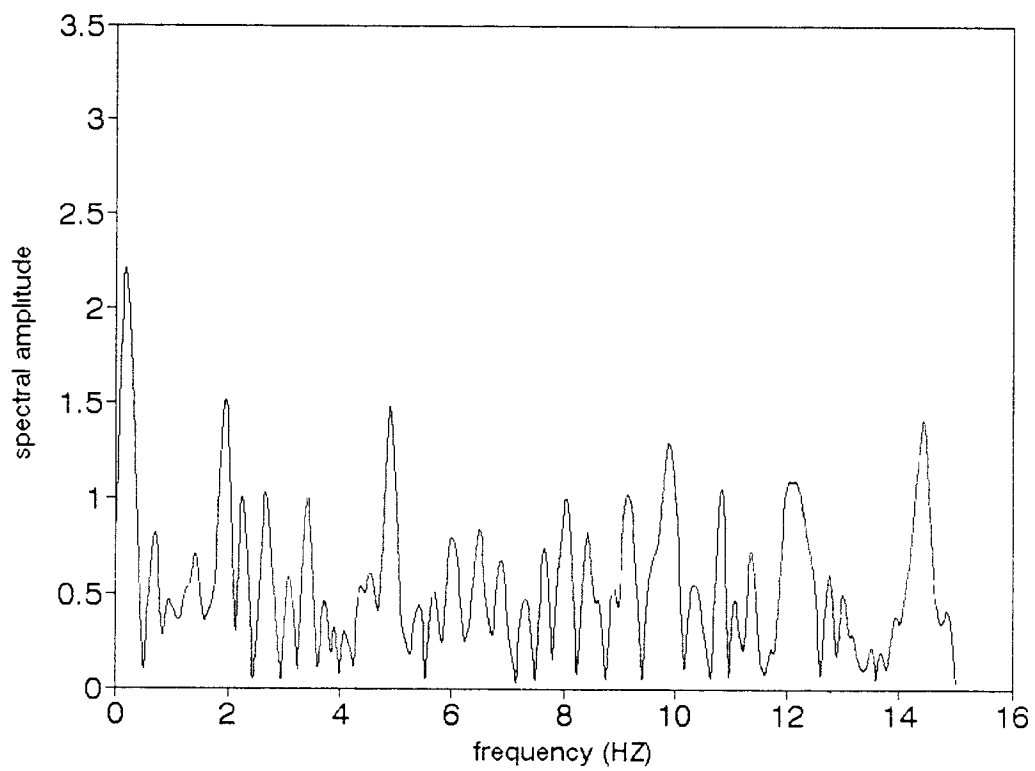


Figure 3.10: FFT of signal $y_3(n)$

this case, percent air in concrete is equal to 4.03.

Gain in an electronic system, such as an amplifier, is adjusted so that the output of the system does not exceed the linear input range of any other device that it would be connected to. For instance, the analog to digital converter at the output end of the amplifier, and the input end of the computer operates at a maximum range of $\pm 5\text{v}$. Depending on the intensity of acquired signal, the gain in the amplifier is set in such a way so as to keep the voltage input to the computer interface within the linear range ($-5\text{v} \leq \text{input} \leq +5\text{v}$). As shown in the Figure 3.12, in a high gain system, a minute change in signal can easily place the output signal in the saturated or nonlinear range. On the other hand, in a properly designed instrument, the gain is set at such a range so that for the level input signals encountered, the output is not saturated. However, it is desirable to have the gain at an optimal level so as to operate with high sensitivity while the output is not exceeding the saturated level. The present system's gain is set at an optimum level so that while the level of signal magnification is high, it is not too high for the signals to be saturated. Figure 3.13 compares the output characteristics of a system with a normal gain setting and another system operating at very high gain. In the normal gain system signal amplitude changes according to the size of an individual air bubble (the amount of time the sensor spends inside a bubble), as the sensor is traversed in concrete. Amplified signal will never reach the calibrated open air level, unless it encounters a very large bubble. However, the response is within the linear range and the area under the signal response curve can be directly related to the amount of air the sensor has encountered. On the other hand, in a high gain system, the output signal will reach the saturated level even for even extremely small bubbles. Once a signal reaches the nonlinear saturated level, their response can no longer be

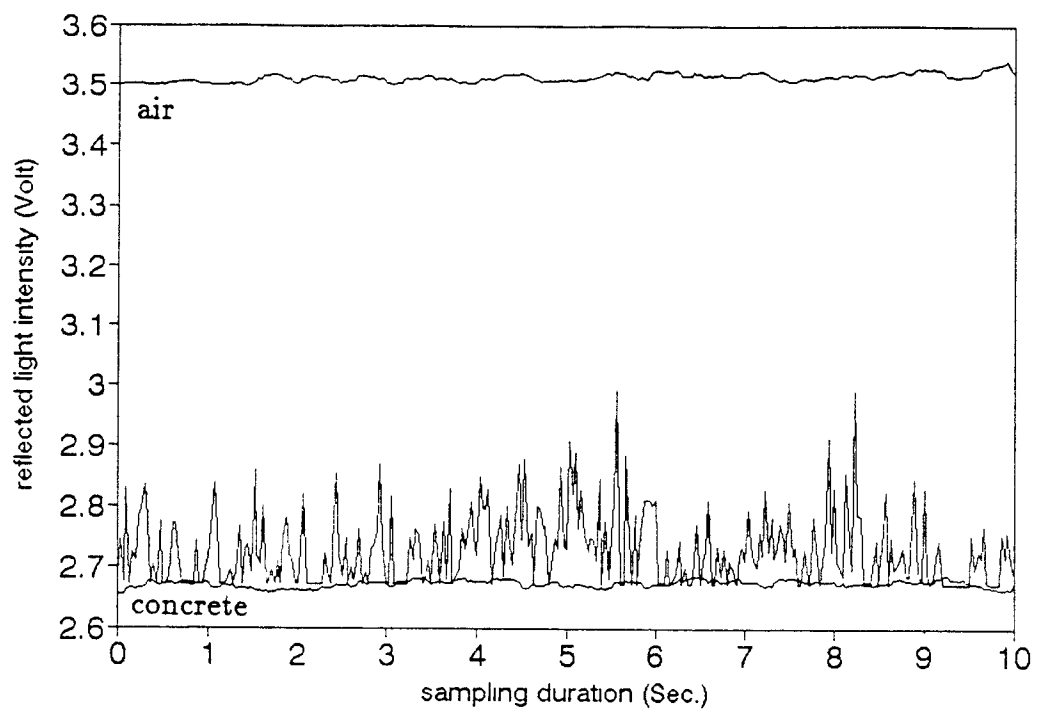


Figure 3.11: Example of one experiment test data calibration

directly related to the air bubble size, since the system does not behave in a linear fashion.

Signal processing and calibration calculation procedures are performed automatically through the Lotus 123 spreadsheet (Macro) program. In this program, three data files are called after acquisition of data by LABETECH ACQUIRE software. These files include the test data, as well as the air and concrete reference files. Test result and the plot of reflected light intensity versus time is displayed after executing this program. Program list is provided in Appendix F.

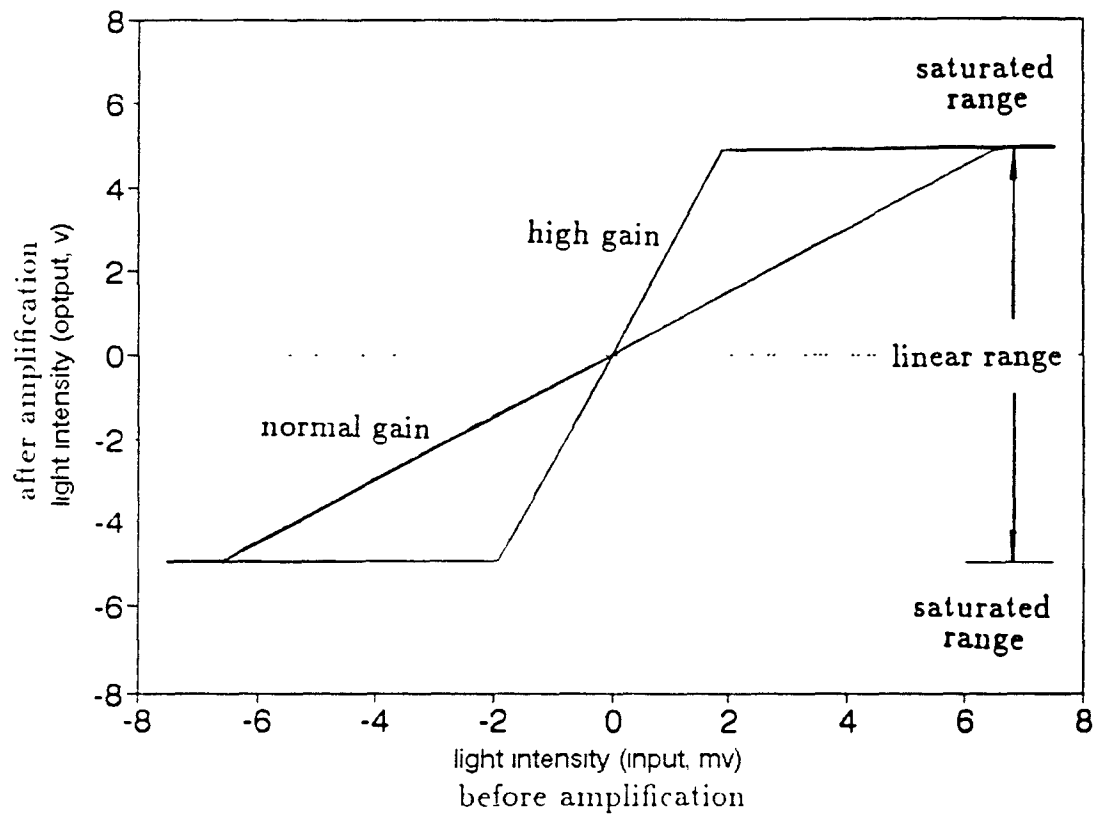


Figure 3.12: Amplifier gain effect on signal range

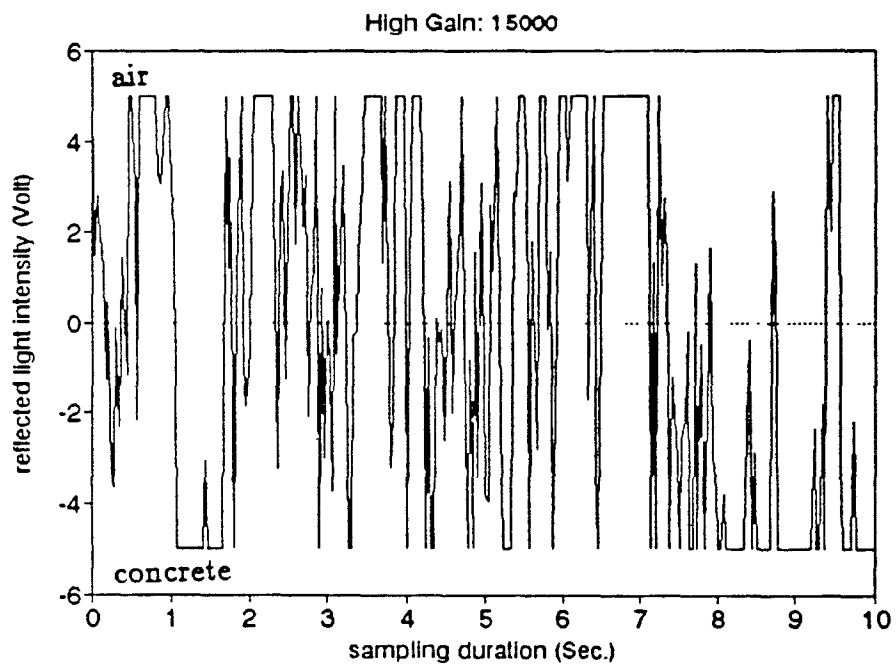
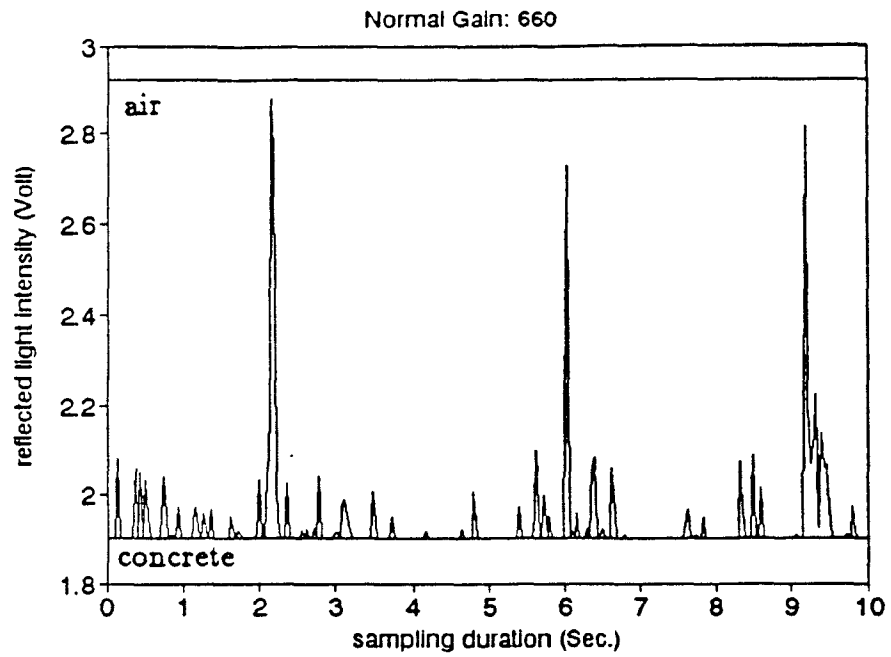


Figure 3.13: Two test data using different amplifier gain in same concrete

Chapter 4

Experimental Results and Discussion

4.1 Experiment Sampling and Testing

Air percent in fresh concrete was controlled by using an air entraining admixture (MB-VR) manufactured by Master Builders. By varying the amount of MB-VR added to each mix, a range of mixes with varying percentages of air were obtained.

Three devices were used to determine the entrained air percentage:

- Precision Air Entrainment Meter (Model CT 126-A, manufactured by Soiltest, pressure meter)
- Roll-a-meter (volumetric meter, manufactured by Soiltest)
- Fiber Optic System

Experimental program consisted of three major portions: (1) prefield labora-

tory tests, (2) field trials, (3) laboratory tests with improved probe head.

4.2 Laboratory Results

The fiber optic sensor with the syringe needle head was employed in laboratory experiments. A concrete mix proportion of 1 : 1.5 : 1.5 : 0.55 (cement : sand : aggregate : water) by weight was employed, and the amount of air entraining admixture was varied for each batch. In these experiments, The syringe needle probe was moved around the large aggregate particles in plastic concrete. In this way, the needle could easily detect air bubbles in the paste, without being disturbed by the presence of large aggregates. For comparison, the pressure and the roll-a-meter instruments were also employed for measurement of the air content on the same batches of concrete. For the fiber optic method, three measurements were taken in each test. The average of these three tests was used for comparison with the other two methods. Experimental results are listed in the Table 4.1. As it is shown in Figure 4.1, average of the fiber optic results compare very well with the other two methods.

4.3 Field Trials

The fiber optic sensor system was also employed at several highway construction sites. Sites were located in various states including New York, Pennsylvania and Minnesota. Earlier experiments in Pennsylvania and New York indicated that the sensor tip could be easily damaged by the stiff highway concrete mix, and large aggregates (nominal diameter of $1\frac{1}{2}$ "). Several attempts were then made for de-

<i>Volume of MB-VR Add</i> (ml MB-VR / 100 kg cement)	<i>Percentage of Air Entrainment</i>			
	Pressure Meter	Volumetric Meter	Data File Name	Fiber Optic Reading
5.4	2.1	2.6	N16D.DAT N16E.DAT N16F.DAT	2.47 2.34 1.94 2.25 (Avg)
10.8	3.3	3.6	N28G.DAT N28H.DAT N28L.DAT	3.41 3.02 3.22 3.19 (Avg)
16.3	3.6	3.6	N28O.DAT N28P.DAT N28Q.DAT	3.28 2.97 3.52 3.25 (Avg)
21.7	3.8	3.4	N27O.DAT N27P.DAT N27Q.DAT	3.55 3.49 3.55 3.53 (Avg)
32.5	4.7	4.5	N27U.DAT N27K.DAT N27L.DAT	3.80 4.03 4.03 3.95 (Avg)
43.3	4.9	5.0	D8G.DAT D8H.DAT D8I.DAT	5.31 4.99 4.71 5.00 (Avg)
48.8	6.6	6.8	D4J.DAT D4Y.DAT D4L.DAT	6.40 6.71 6.17 6.42 (Avg)

Table 4.1: Test results

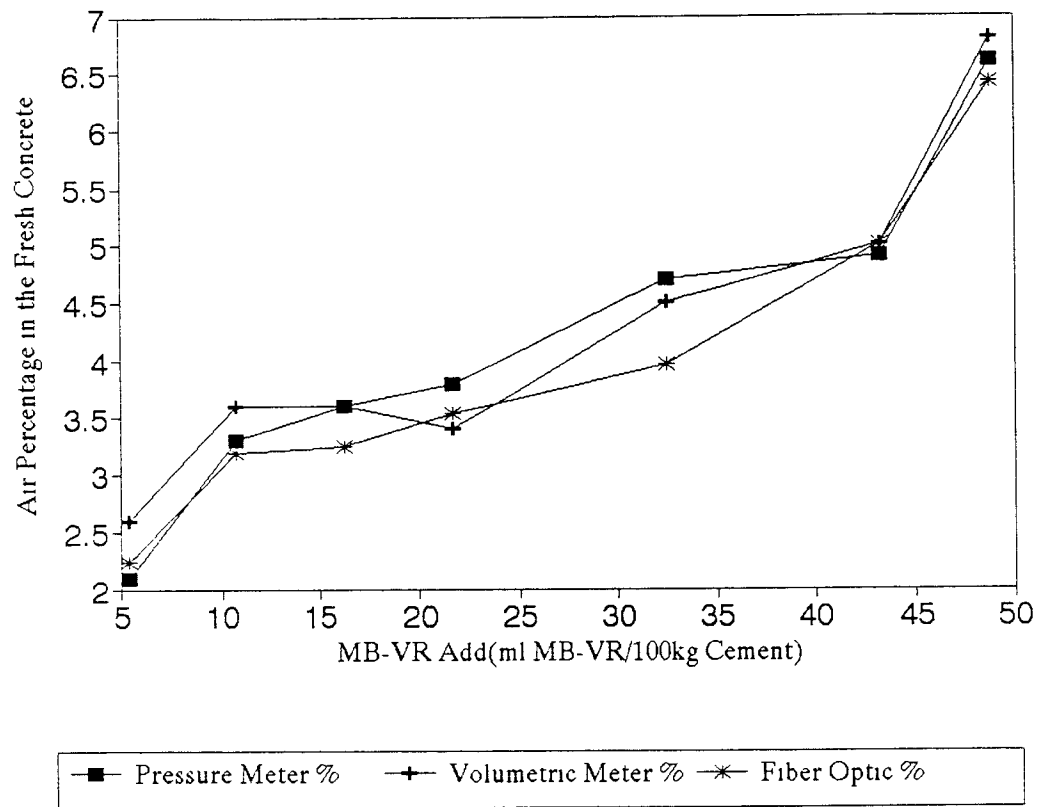


Figure 4.1: Three test methods comparison

<i>Location</i>	<i>Date</i>	<i>Fiber Optic Reading</i>	<i>Pressure Meter</i>
Mount Kisko, New York	Aug.23, 1990	3.83 3.87 4.42 4.04 (Avg)	4.0
I-80 in PA, NJ-PA Border	Jun.15, 1990	6.23 7.36 6.17 6.59 (Avg)	6.8
Labanon County, Pennsylvania	Aug.28, 1990	5.79 5.48 5.65 5.64 (Avg)	6.0
Moorhead, Minnesota (Low Air Concrete)	Aug.27, 1990	3.31 3.22 4.93 3.82 (Avg)	3.7 (Roll-A-Meter)
Moorhead, Minnesota (Wheel Barrel Test)	Sept.18, 1990	6.32 6.89 5.99 6.40 (Avg)	5.7
Moorhead, Minnesota (Slab Test)	Sept.18, 1990	5.74 4.95 5.71 5.47 (Avg)	5.3

Table 4.2: Field Test Data

signing a suitable protective head for the sensor tip. The final design consists of a U-shaped aluminum head (Figure 4.2) to repel the large aggregates that come in contact with the sensor. Fiber optic field test results and the corresponding pressure meter values from trials in New York, Pennsylvania and Minnesota are given in Table 4.2.

Some laboratory tests were carried with improved probe head. The test results are shown in Tables 4.3, 4.4, 4.5, 4.6.

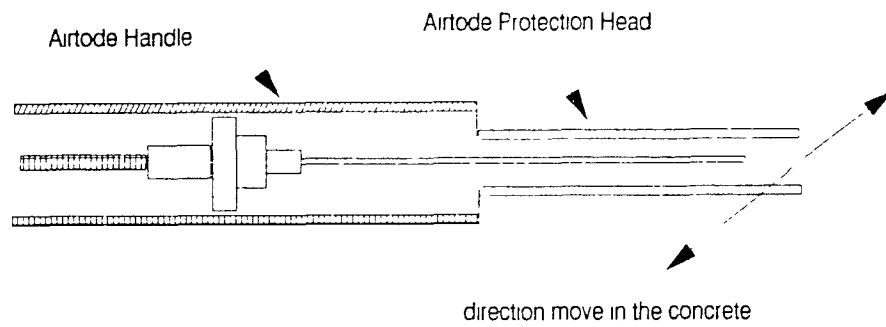


Figure 4.2: U-shaped sensor protection head

<i>Data File Name</i>	<i>Fiber Optic Reading</i>	<i>Pressure Meter</i>	<i>Probe Head Shape</i>
A14-1.WK1	4.75	4.5	U-Shape
A14-2.WK1	5.34		U-Shape
A14-3.WK1	4.53		U-Shape
A14-4.WK1	4.18		U-Shape
A14-5.WK1	4.37		U-Shape
A14-6.WK1	5.08		U-Shape
A14-7.WK1	4.61		U-Shape
A14-8.WK1	4.44		U-Shape
A14-9.WK1	5.03		U-Shape
A14-10.WK1	4.54		U-Shape
Average:	4.69		

Table 4.3: Laboratory tests results (1) with improved probe head

<i>Data File Name</i>	<i>Fiber Optic Reading</i>	<i>Pressure Meter</i>	<i>Probe Head Shape</i>
A15-1.WK1	3.27	3.2	U-Shape
A15-2.WK1	3.68		U-Shape
A15-3.WK1	3.32		U-Shape
A15-4.WK1	4.22		U-Shape
A15-5.WK1	2.89		U-Shape
A15-6.WK1	4.16		U-Shape
A15-7.WK1	3.19		U-Shape
A15-8.WK1	4.26		U-Shape
A15-9.WK1	3.51		U-Shape
A15-10.WK1	3.71		U-Shape
Average:	3.62		

Table 4.4: Laboratory tests results (2) with improved probe head

4.4 Air Bubble Numbers and Size Analysis

Determination of air bubble size distribution is even more important than measurement of total air content. One way of determining the air bubble size distribution is by microscopic analysis of hardened concrete. In another parallel study [18], an automated image analysis system is employed for the study of air bubble size distribution.

In the fiber optic system, the higher the amplitude, the larger the air bubble size. The effect of bubble size and spacing on the amplitude of reflected light signal is shown in Figure 4.3.

An experimental program was designed for the analysis of air bubble size distribution by the fiber optic and the image analysis methods. Four different batches with varying amounts of MB-VR and a mix proportion of 1 : 2.1 : 3.7 : 0.5 by weight of cement : sand : aggregate : water were prepared. A prism of $4'' \times 4'' \times 12''$ was cast with each batch for later microscopic analysis. Air content in each batch was measured by the pressure and the fiber optic methods, for which the results are shown in the Table 4.8, 4.9, 4.10 and 4.11. As shown in these tables, ten fiber optic readings were taken for each pressure reading. Hardened concrete prisms were cut into thin slices ($3/8$ inch thick) after two weeks by diamond wheel saw for microscopic analysis.

Early experimental results indicate existence of a correlation between the air bubble size distribution obtained by microscopic analysis and the fiber optic method. Relative air bubble size values are determined as the difference in between the amplitude of the test signal and the baseline. These relative size values are given

<i>Data File Name</i>	<i>Fiber Optic Reading</i>	<i>Pressure Meter</i>	<i>Probe Head Shape</i>
A16-1.WK1	4.45	6.2	Spring-Shape
A16-2.WK1	5.96		Spring-Shape
A16-3.WK1	6.02		Spring-Shape
A16-4.WK1	5.52		Spring-Shape
A16-5.WK1	6.57		Spring-Shape
A16-6.WK1	6.23		U-Shape
A16-7.WK1	5.76		U-Shape
A16-8.WK1	6.16		U-Shape
A16-9.WK1	5.97		U-Shape
A16-10.WK1	6.62		U-Shape
Average:	5.97		

Table 4.5: Laboratory tests results (3) with improved probe head

<i>Data File Name</i>	<i>Fiber Optic Reading</i>	<i>Pressure Meter</i>	<i>Probe Head Shape</i>
A17-1.WK1	5.22	5.2	Spring-Shape
A17-2.WK1	5.47		Spring-Shape
A17-3.WK1	4.41		Spring-Shape
A17-4.WK1	4.97		Spring-Shape
A17-5.WK1	4.77		Spring-Shape
A17-6.WK1	4.33		Spring-Shape
A17-7.WK1	5.82		Spring-Shape
A17-8.WK1	4.13		Spring-Shape
A17-9.WK1	5.80		Spring-Shape
A17-10.WK1	5.18		Spring-Shape
Average:	5.01		

Table 4.6: Laboratory tests results (4) with improved probe head

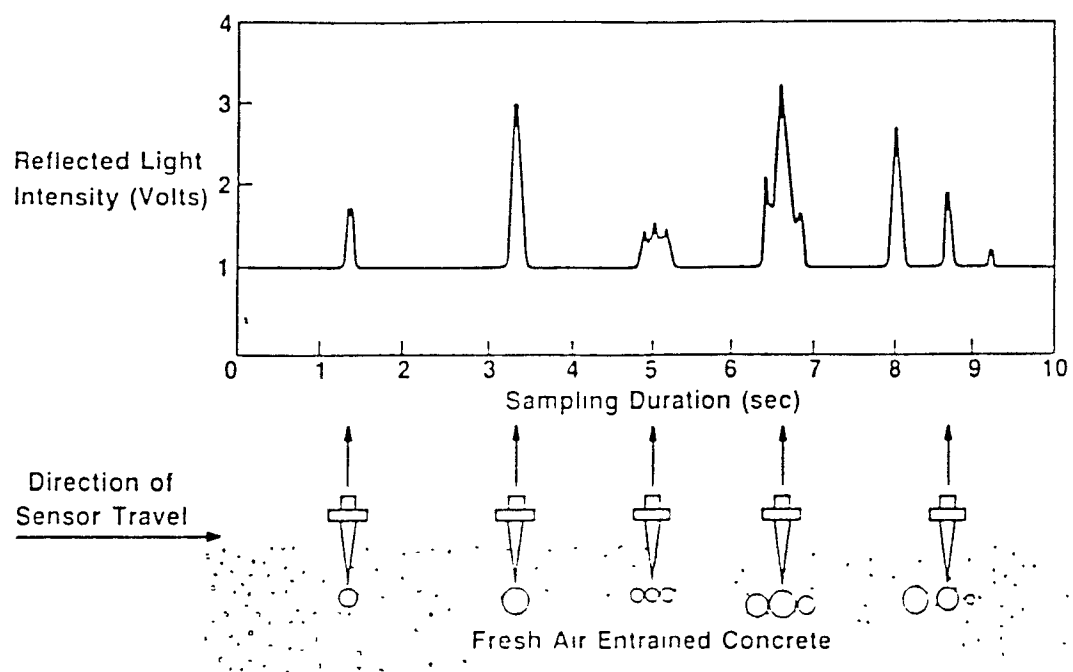


Figure 4.3: Effect of bubble size and spacing on the amplitude of reflected light signal

<i>Group</i>	<i>Amplitude Range (relative)</i>	
very very small air bubble	0 - 0.05	volts
very small air bubble	0.05 - 0.075	volts
small air bubble	0.075 - 0.10	volts
medium air bubble	0.10 - 0.15	volts
large air bubble	0.15 - 0.20	volts
very large air bubble	≥ 0.20	volts

Table 4.7: Air bubble size groups

in volt units, and can be divided into a few groups representing range of sizes as shown in Table 4.7.

For example, size range analysis of two sets of samples as shown in Table 4.12 and 4.13 indicates the number of air bubbles in each size range. Figure 4.4 and 4.6 show the results of the fiber optic analysis method from Table 4.12 and 4.13. Figure 4.5 and 4.7 show the results from the microscopic analysis of hardened concrete from the same samples. As can be seen from Figure 4.5 (test sample one), the concrete had no entrained air, only entrapped air, that is because no air entraining agent had been added. Whereas an air entraining agent had been added to the concrete (test sample two). The air entraining agent produces stable air bubbles of small diameter dispersed throughout the concrete. Thus concrete which is air entrained has a much large number of small air bubble.

The length of traverse in fresh concrete by the fiber optic method was a little less than 20 inches for a time interval of 10 seconds. In the case of hardened concrete, the length of traverse on each slice was 12.57 inches and the total length of traverse was 100 inches on the whole sample. The length of traverse for fiber optic is closer to the length traversed on a single slice, hence results from the fiber optic method should be compared with those of single slices shown in Figure 4.8, 4.9, 4.10, 4.11,

<i>Data File Name</i>	<i>Fiber Optic Reading</i>	<i>Pressure Meter Reading</i>
2F1.WK1	2.22	2.2
2F2.WK1	2.49	
2F3.WK1	2.42	
2F4.WK1	2.45	
2F5.WK1	2.43	
2F6.WK1	2.32	
2F7.WK1	2.32	
2F8.WK1	2.27	
2F9.WK1	2.23	
2F10.WK1	2.04	
Average:	2.32	

Table 4.8: Experiment data for air bubble size analysis (1)

<i>Data File Name</i>	<i>Fiber Optic Reading</i>	<i>Pressure Meter Reading</i>
3F1.WK1	3.87	4.0
3F2.WK1	4.37	
3F3.WK1	5.80	
3F4.WK1	4.52	
3F5.WK1	4.87	
3F6.WK1	3.77	
3F7.WK1	4.40	
3F8.WK1	3.88	
3F9.WK1	5.00	
3F10.WK1	3.87	
Average:	4.43	

Table 4.9: Experiment data for air bubble size analysis (2)

4.12, 4.13, 4.14 and 4.15, (for test sample two), rather than the final result shown in Figure 4.7. More studies need to be done to establish further correlation between these two methods.

<i>Data File Name</i>	<i>Fiber Optic Reading</i>	<i>Pressure Meter Reading</i>
5F1.WK1	4.96	5.0
5F2.WK1	5.96	
5F3.WK1	5.72	
5F4.WK1	5.89	
5F5.WK1	4.67	
5F6.WK1	4.86	
5F7.WK1	5.10	
5F8.WK1	6.23	
5F9.WK1	6.19	
5F10.WK1	5.57	
Average:	5.53(Avg)	

Table 4.10: Experiment data for air bubble size analysis (3)

<i>Data File Name</i>	<i>Fiber Optic Reading</i>	<i>Pressure Meter Reading</i>
6F1.WK1	4.96	6.3
6F2.WK1	5.17	
6F3.WK1	6.15	
6F4.WK1	5.92	
6F5.WK1	5.23	
6F6.WK1	6.61	
6F7.WK1	5.62	
6F8.WK1	7.68	
6F9.WK1	7.26	
6F10.WK1	5.95	
Average:	6.06	

Table 4.11: Experiment data for air bubble size analysis (4)

Data File Name	<i>Air Bubble Number and Size</i>					
	Very Very Small Air Bubble No.	Very Small Air Bubble No.	Small Air Bubble No.	Medium Air Bubble No.	Large Air Bubble No.	Very Large Air Bubble No.
2F1.WK1	117	70	45	37	2	0
2F2.WK1	126	62	65	29	1	2
2F3.WK1	105	81	56	36	2	0
2F4.WK1	111	66	67	35	0	0
2F5.WK1	109	79	58	37	1	0
2F6.WK1	115	72	44	36	4	0
2F7.WK1	130	66	60	29	1	0
2F8.WK1	106	89	40	28	1	3
2F9.WK1	141	74	47	22	1	2
2F10.WK1	136	69	46	25	0	0
Average:	120	73	31	31	1.3	0.7

Table 4.12: Air bubble number and size for test sample one

Data File Name	<i>Air Bubble Number and Size</i>					
	Very Very Small Air Bubble No.	Very Small Air Bubble No.	Small Air Bubble No.	Medium Air Bubble No.	Large Air Bubble No.	Very Large Air Bubble No.
3F1.WK1	110	68	48	32	3	1
3F2.WK1	122	71	53	38	4	2
3F3.WK1	133	72	49	36	3	1
3F4.WK1	126	63	64	29	3	1
3F5.WK1	123	61	58	34	2	2
3F6.WK1	108	73	41	39	2	0
3F7.WK1	128	63	48	28	2	0
3F8.WK1	124	68	52	31	3	2
3F9.WK1	132	81	41	29	4	1
3F10.WK1	115	72	56	33	3	1
Average:	122	69	51	33	3	1.1

Table 4.13: Air bubble number and size for test sample two

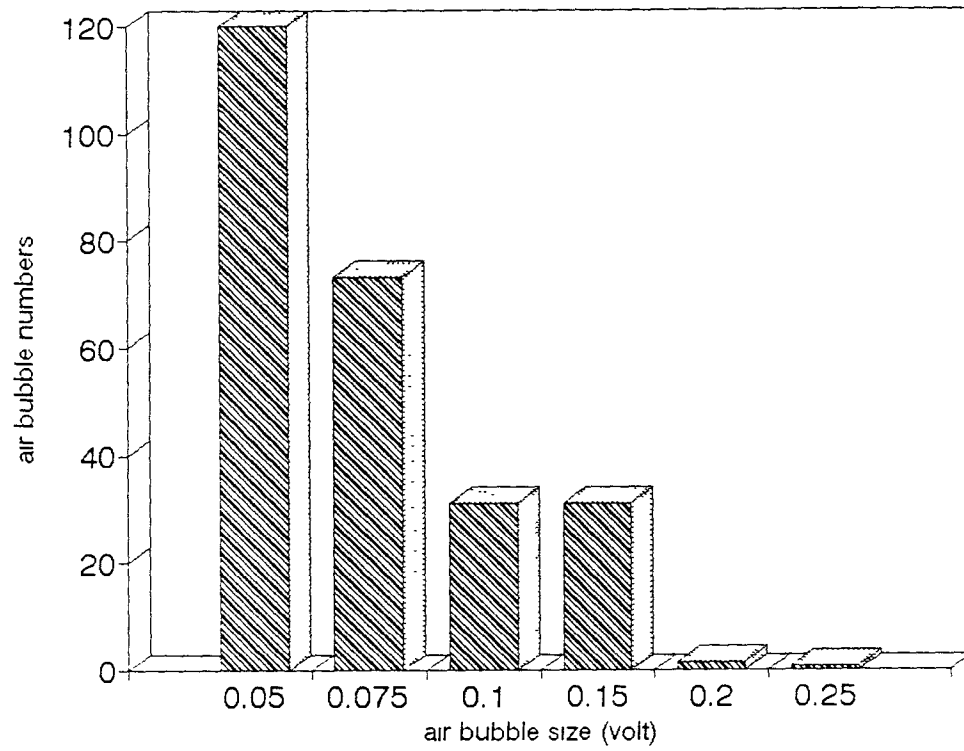
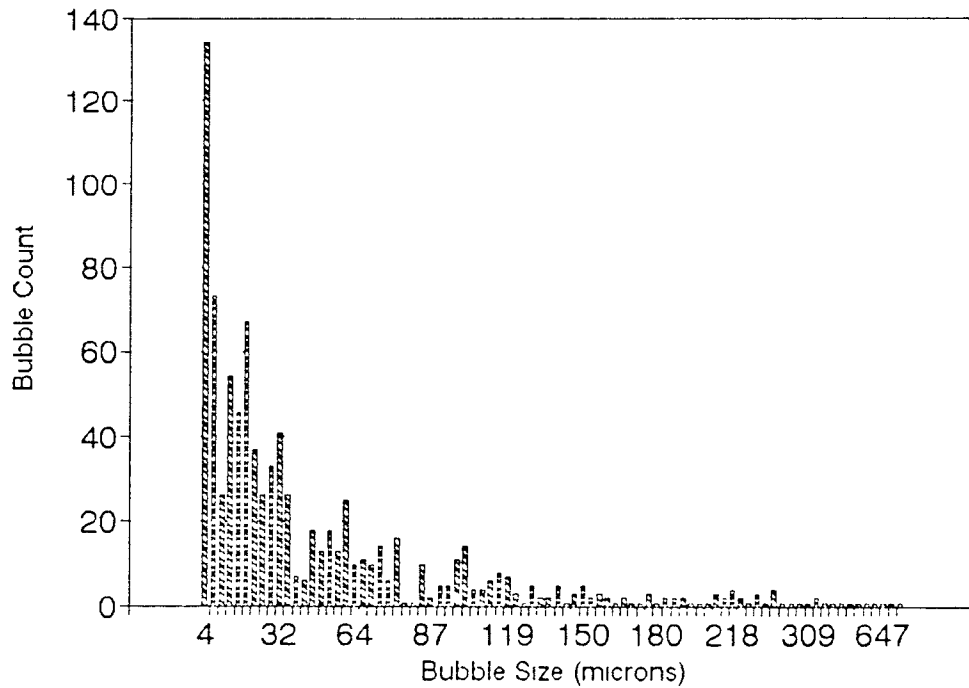


Figure 4.4: Air bubble size and numbers in concrete analysis using fiber optic method for test sample one



Total Length of Traverse : 2553.6 mm (100.5 inches)
 Number of Air Bubbles intercepted : 975
 Sum Of Bubble Lengths : 52.571 mm
 Air void Content : 2.06%

Figure 4.5: Air bubble size and numbers in concrete analysis using microscopic method for test sample one

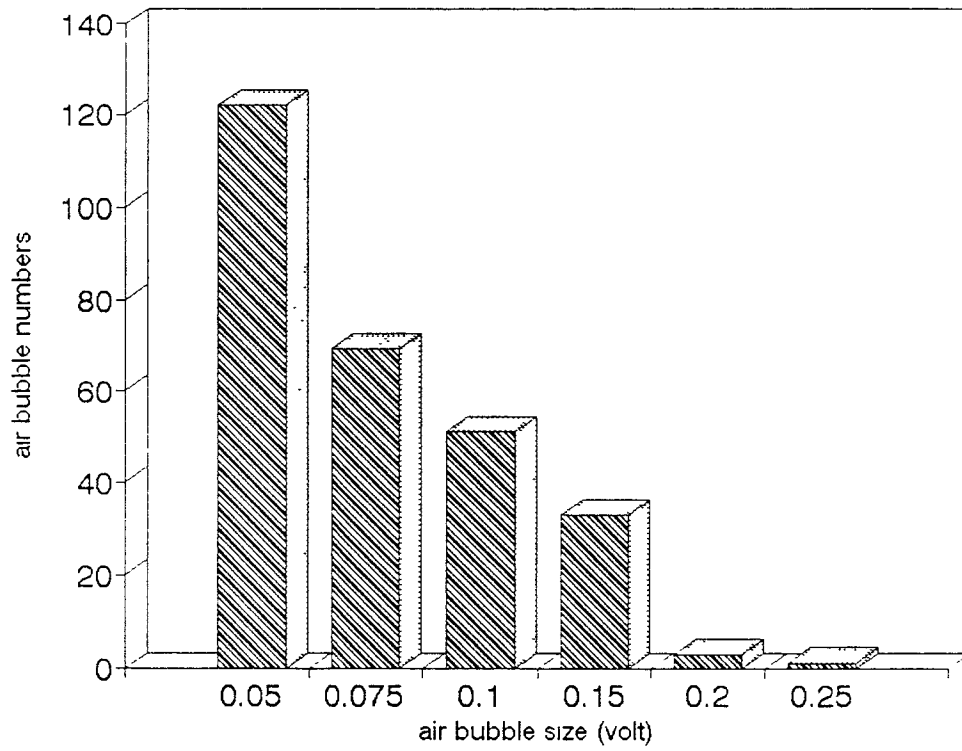
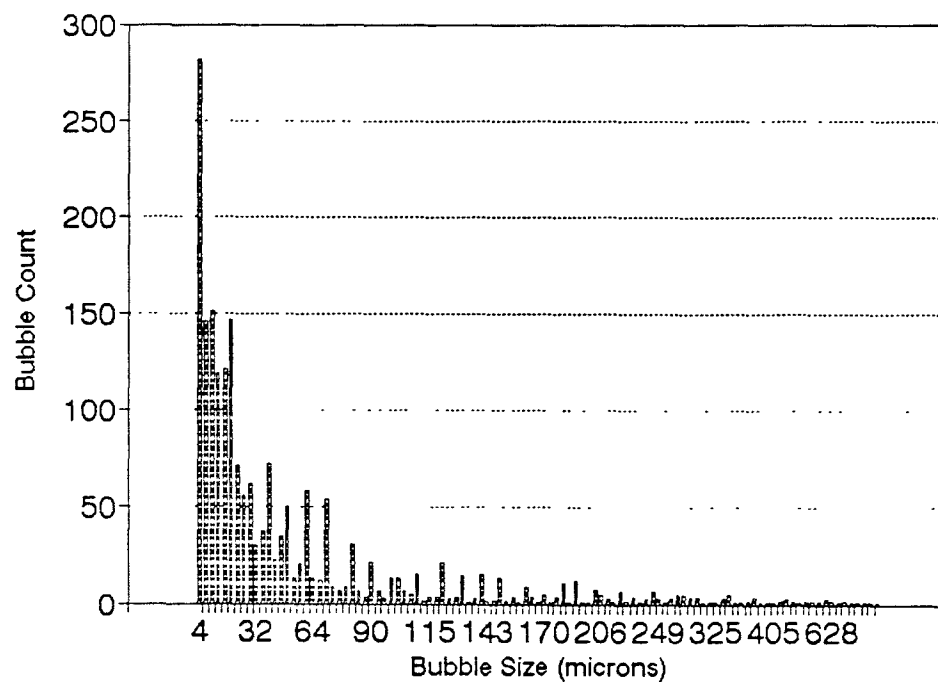
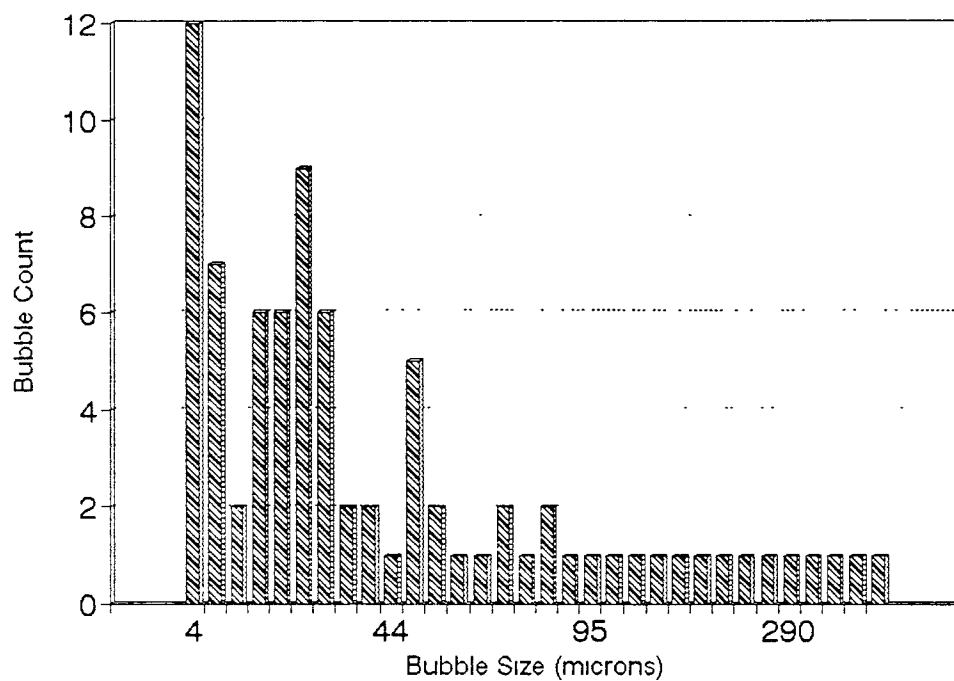


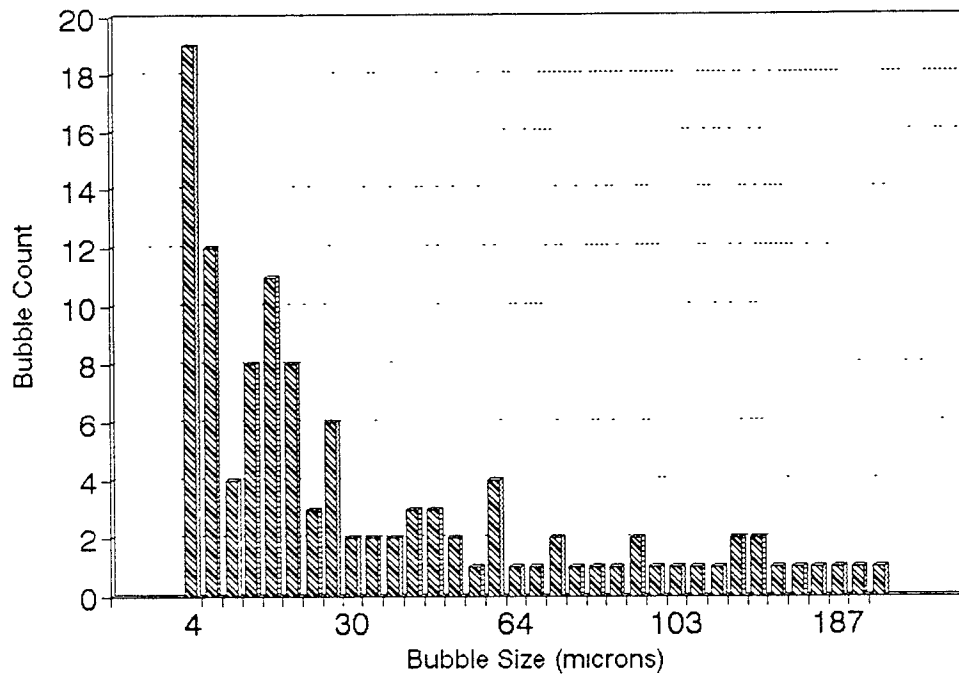
Figure 4.6: Air bubble size and numbers in concrete analysis using fiber optic method for tset sample two



Total Length of Traverse : 2553.6 mm (100.5 inches)
 Number of Air Bubbles intercepted : 1832
 Sum Of Bubble Lengths : 109.68 mm
 Air void Content : 4.29 %

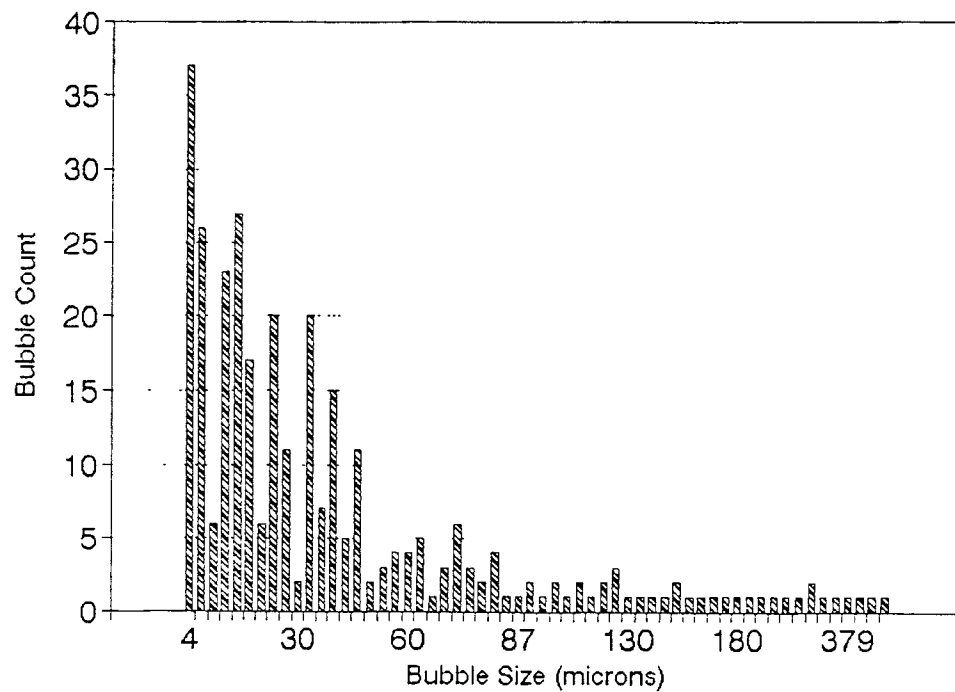
Figure 4.7: Air bubble size and numbers in concrete analysis using microscopic analysis method for test sample two





TOTAL LENGTH TRAVERSED : 319.20 mm= 12.57 in
 NUMBER OF AIR BUBBLES : 113
 TOTAL LENGTH OF AIR BUBBLES : .46778660E+01mm
 TOTAL LENGTH OF CHORD : 14948900E+03mm
 AIR VOID CONTENT 1.4655%

Figure 4.9: Air bubble size and number in concrete analysis using microscopic analysis method for test sample two slice (2)



TOTAL LENGTH TRAVERSED . 319.20 mm = 12.57 in
 NUMBER OF AIR BUBBLES . 310
 TOTAL LENGTH OF AIR BUBBLES : .14611540E+02mm
 TOTAL LENGTH OF CHORD .13956330E+03mm
 AIR VOID CONTENT 4.5775%

Figure 4.10: Air bubble size and number in concrete analysis using microscopic analysis method for test sample two slice (3)

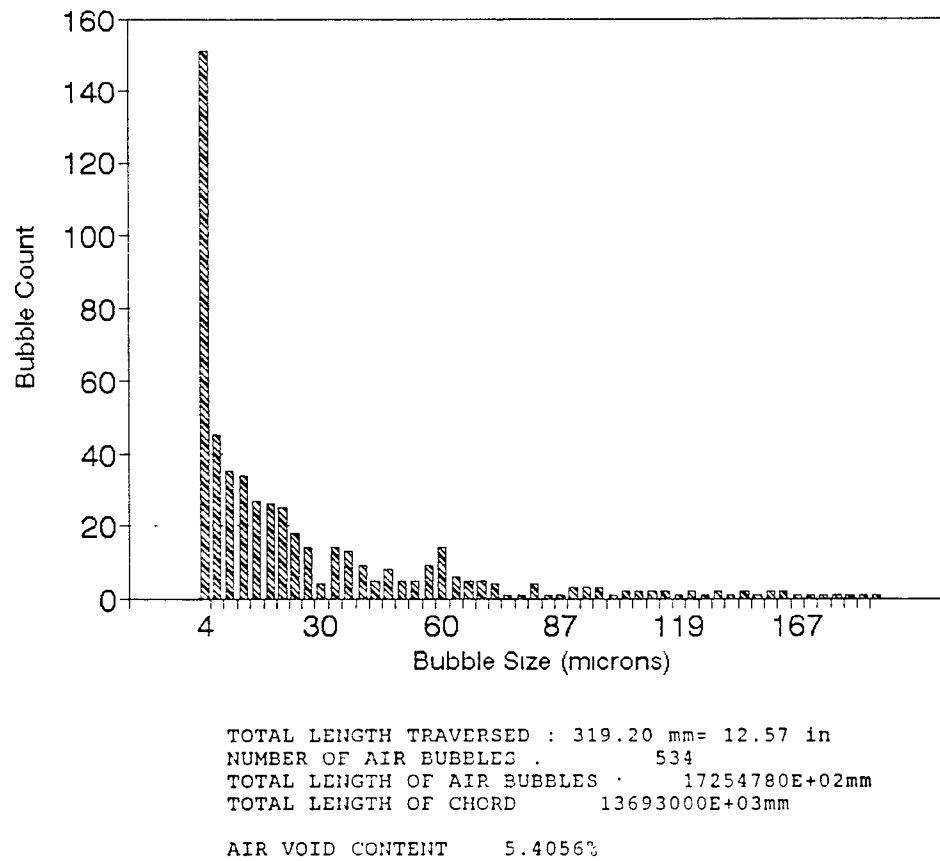
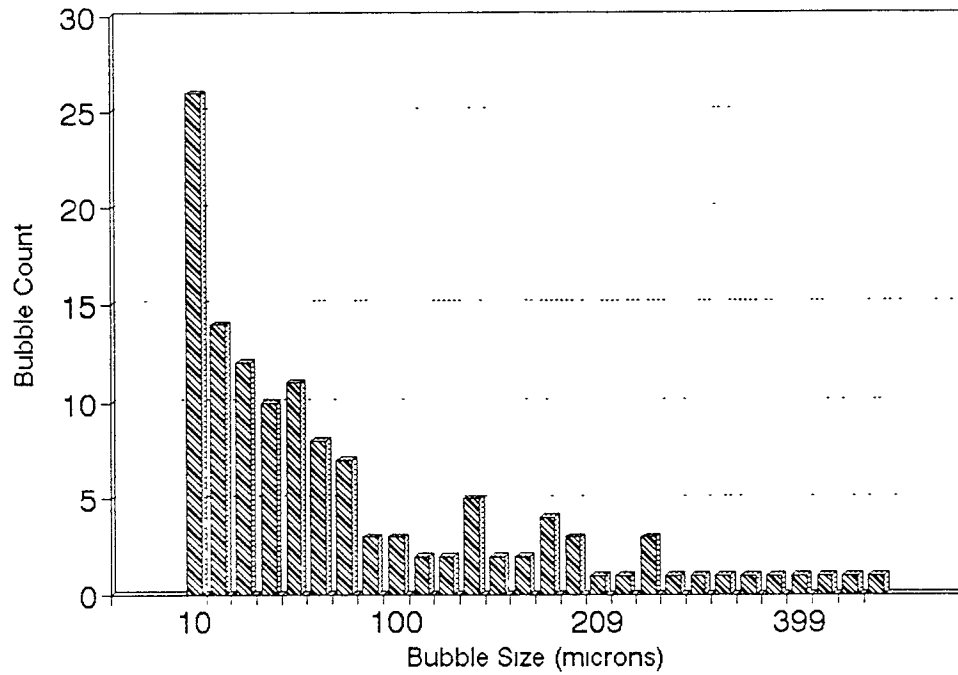


Figure 4.11: Air bubble size and number in concrete analysis using microscopic analysis method for test sample two slice (4)



TOTAL LENGTH TRAVERSED . 319.20 mm= 12.57 in
 NUMBER OF AIR BUBBLES . 132
 TOTAL LENGTH OF AIR BUBBLES . 13265150E+02mm
 TOTAL LENGTH OF CHORD .30531790E+03mm
 AIR VOID CONTENT 4.1557%

Figure 4.12: Air bubble size and number in concrete analysis using microscopic analysis method for test sample two slice (5)

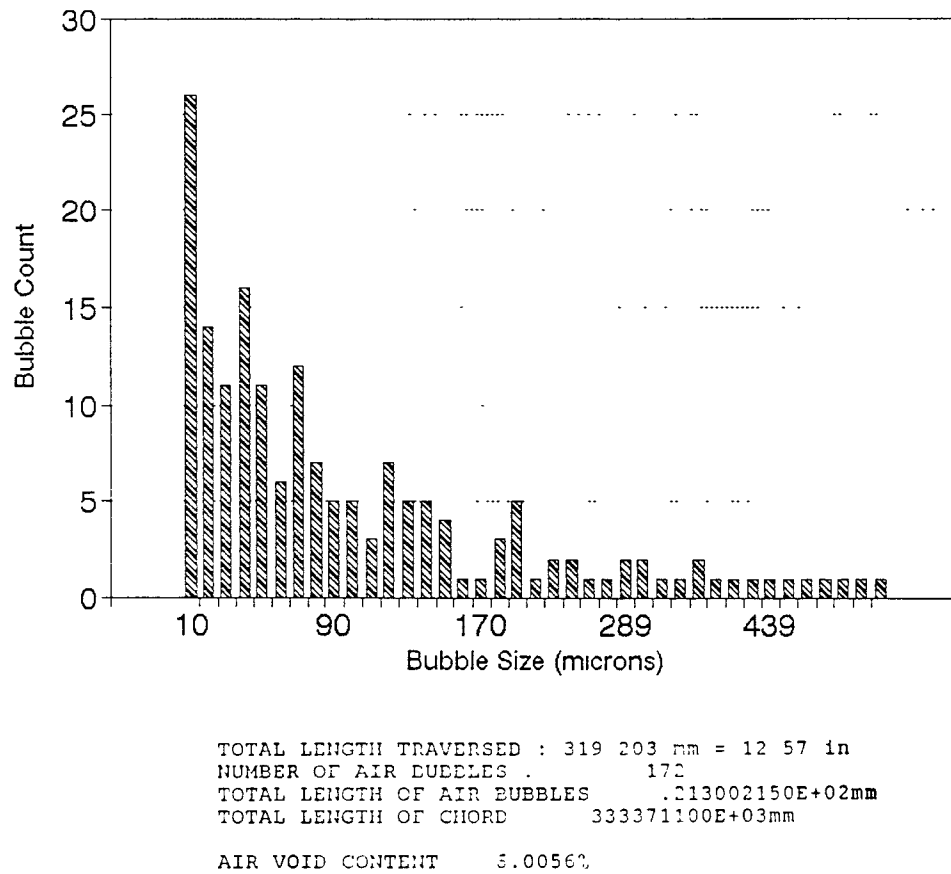
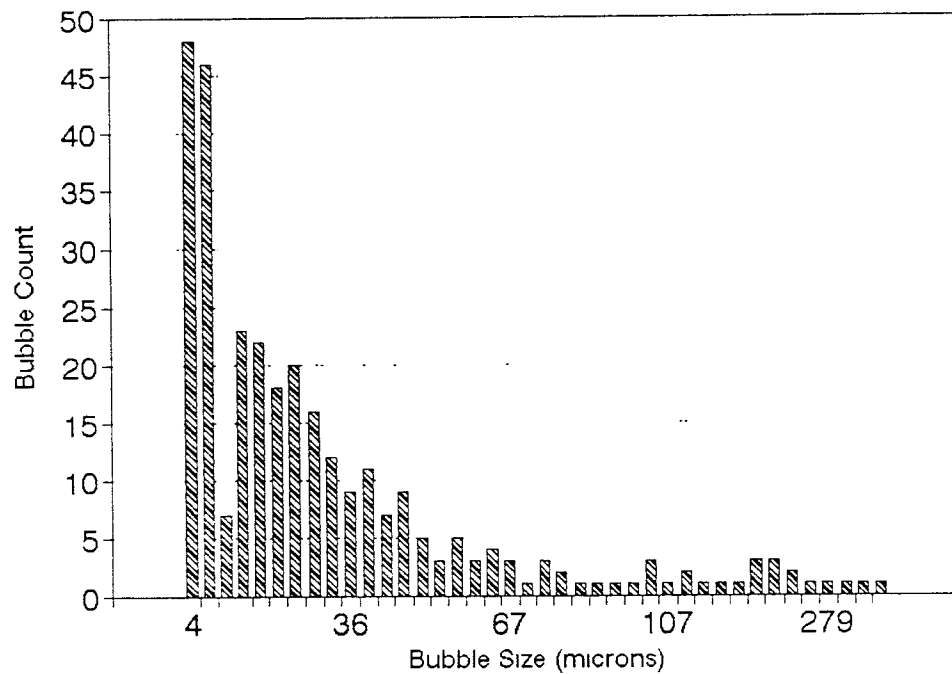
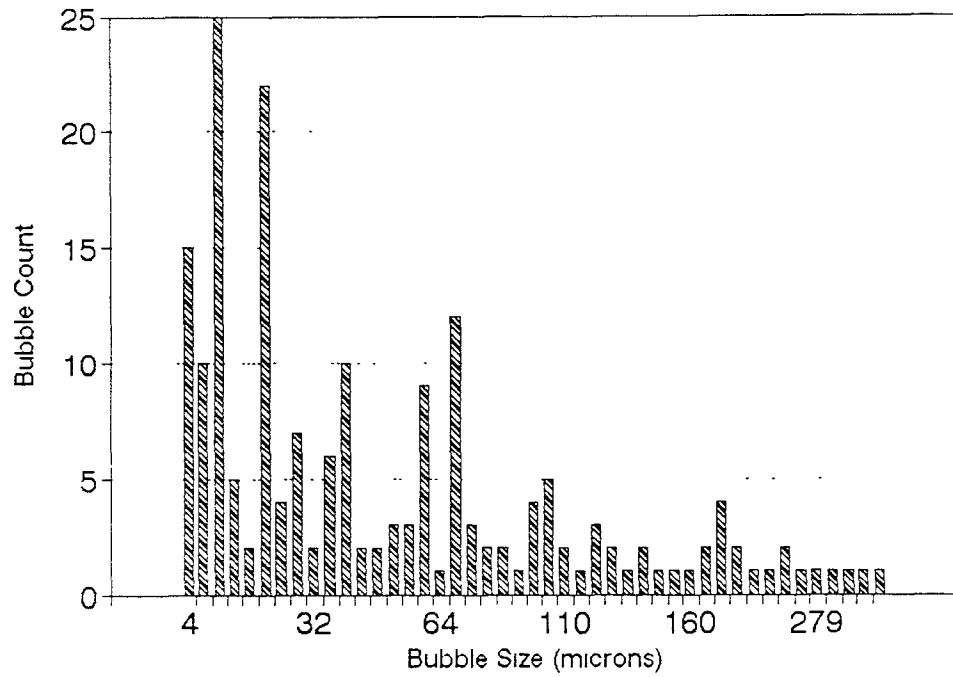


Figure 4.13: Air bubble size and number in concrete analysis using microscopic analysis method for test sample two slice (6)



TOTAL LENGTH TRAVERSED 319.30 mm = 12.57 in
 NUMBER OF AIR BUBBLES 304
 TOTAL LENGTH OF AIR BUBBLES .10827800E+02mm
 TOTAL LENGTH OF CHORD 14224300E+03mm
 AIR VOID CONTENT 3.32200

Figure 4.14: Air bubble size and number in concrete analysis using microscopic analysis method for test sample two slice (7)



TOTAL LENGTH TRAVERSED 319.20 mm= 12.57 in
 NUMBER OF AIR BUBBLES 183
 TOTAL LENGTH OF AIR BUBBLES .12120620E+02mm
 TOTAL LENGTH OF CHORD .23229310E+03mm
 AIR VOID CONTENT 0.39720

Figure 4.15: Air bubble size and number in concrete analysis using microscopic analysis method for test sample two slice (8)

4.5 Conclusions

Development of a multimode fiber optic air bubble detection system in fresh concrete is presented. This concept suggests an alternative way of solving the problem of measuring entrained air content in fresh concrete. However, several technical difficulties as yet have to be solved:

- Fiber optic sensor head protection
- Fiber optic sensor to directional coupler connection

A good fiber optic sensor in this system is defined as having sufficient range and quick response. So, if the fiber optic sensor is well polished, it should be kept in a well protected condition. At present, it is difficult to reach that point after several tests, usually the sensor needs to be polished again.

When the fiber optic sensor is connected to the directional coupler, an index matching epoxy epo-tek 394 manufactured by Epoxy Technology Inc. is needed. The connection causes some losses in the signal.

In the case of the work done in this thesis, some problems have been observed, and as such they can provide opportunity for future research. A pulse laser can be employed so that the data acquisition can be done digitally. In this way, some of the present system's difficulties may be reduced. For example, the sensor's range and sensitivity will not affect the output signal. Instead of a microcomputer, data acquisition can be performed by a dedicated microprocessor so that the device can be design into a very small portable size suitable for field use.

Bibliography

- [1] Takashi Nakayama. "Optical Sensing Technologies by Multimode Fibers", *Proceedings of 1984 SPIE- The International Society for Optical Engineering*, 1984, pp.19-26.
- [2] T.G.Giallorenzi, etal. "Optical Fiber Sensor Technology", *IEEE Journal on Quantum Electronics*, QE18, 1982, pp.626.
- [3] Max Born. "Principles of Optics", (Fourth Edition), Pergamon Press, 1970, pp.38.
- [4] Shi-Kay Yao and Charles K.Asawa. "Fiber Optical Intensity Sensors", *IEEE Journal on Selected Area in Communications*, vol.SAC-1, No.3, April 1983, pp.562.
- [5] Peter W.Milonni and Joseph H.Eberly, "Laser", Wiley-Interscience, 1988, pp.562-566, pp.550-558.
- [6] Orazio Svelto, "Principles of Lasers", (Third Edition), Plenum Press, 1989.
- [7] Jurgen R.Meyer-Arendt, "Introduction to Classical and Modern Optics", (Third Edition), Prentice Hall, Englewood Cliffs, NJ 1989, pp.13-17.
- [8] Stewart D.Personick, "Fiber Optics Technology and Applications", Plenum Press, 1985, pp.71-91.
- [9] Francis A.Jenkins. "Fundamental of Optics", (Fourth Edition), McGRAW Hill 1976, pp.523-526.
- [10] Newport Corporation, "Instruction Manual of Connector Termination Kit", 1988.
- [11] Newport Corporation, "Projects in Fiber Optics Applications Handbook", 1988.
- [12] Fredrick W.Hughes, "OP-AMP Handbook", (Second Edition), Prentice Hall, Englewood Cliffs, NJ 1986, pp.71.
- [13] Junya Motodate. "Short Wavelength Visible Laser Diode TOLD-9200 Developed by Toshiba has Lasing Wavelength of 670 nm", *JEE*, August 1988, pp.34.

- [14] MetraByte Corporation. "DAS-8 User's Manual", 1988
- [15] Toshiba Corporation. "T1200 Portable Personal Computer User's Manual", 1989.
- [16] Douglas F.Elliott and K.Ramamohan Rao. "Fast Transforms Algorithms, Analyses, Applications", Academic Press, Inc., 1982, pp.58.
- [17] E.Oran Brigham, "The Fast Fourier Transform", Prentice Hall, Englewood Cliffs, NJ 1974, pp.178.
- [18] Sarup Anita, "Image Analysis of Air Void Characteristics in Hardened Concrete", Thesis to be completed, Civil and Environment Engineering, NJIT, Directed by Professor Farhad Ansari.

Appendix A

Laser Diode Technical Data

A.1 TOLD-9200 Features

- Lasing Wavelength: $\lambda_p = 670nm(typ.)$
- Optical Output Power: $P_o = 3mW(CW)$
- Provided with a PIN-PD for Monitoring

A.2 PIN Connection

Figure A.1 shows the PIN connection of TOLD-9200. (Unit in mm)

A.3 Maximum Ratings

See Table A.1.

A.4 Optical-Electrical Characteristics

See Table A.2.

1. LASER DIODE CATHODE
2. LASER DIODE ANODE
PHOTODIODE CATHODE
3. PHOTODIODE ANODE

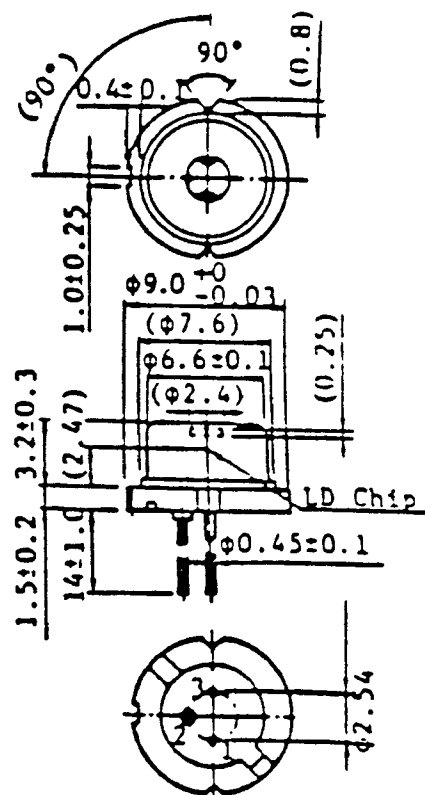


Figure A.1: PIN Connection of TOLD-9200

CHARACTERISTIC	SYMBOL	RATING	UNIT
Optical Output Power	P_O	3	mW
LD Reverse Voltage	$V_R(LD)$	2	V
PD Reverse Voltage	$V_R(PD)$	30	V
Operation Case Temperature	T_C	-10 ~ 50	°C
Storage Temperature	T_{stg}	-40 ~ 65	°C

Table A.1: Maximum Ratings of TOLD-9200 ($T_c = 25^\circ \text{C}$)

CHARACTERISTIC	SYMBOL	TEST CONDITION	MIN.	TYP.	MAX.	UNIT
Threshold Current	I_{th}	CW operating	-	76	90	mA
Operation Current	I_{op}	$P_0 = 2\text{mW}$	-	85	100	mA
Operation Voltage	V_{op}	$P_0 = 2\text{mW}$	-	2.3	3.0	V
Lasing Wavelength	λ_p	$P_0 = 2\text{mW}$	-	670	680	nm
Beam Divergence	$\theta_{//}$	$P_0 = 2\text{mW}$	-	7	-	deg.
	θ_{\perp}	$P_0 = 2\text{mW}$	-	34	-	
Monitor Current	I_m	$P_0 = 2\text{mW}$	0.15	0.45	0.70	mA
PD Dark Current	$I_{D(PD)}$	$V_R = 10\text{V}$	-	-	100	nA
PD Total Capacitance	$C_{T(PD)}$	$V_R=10\text{V}, f=1\text{MHz}$	-	-	20	pF

Table A.2: Optical-Electrical Characteristics of TOLD-9200 ($T_c = 25^\circ \text{C}$)

Appendix B

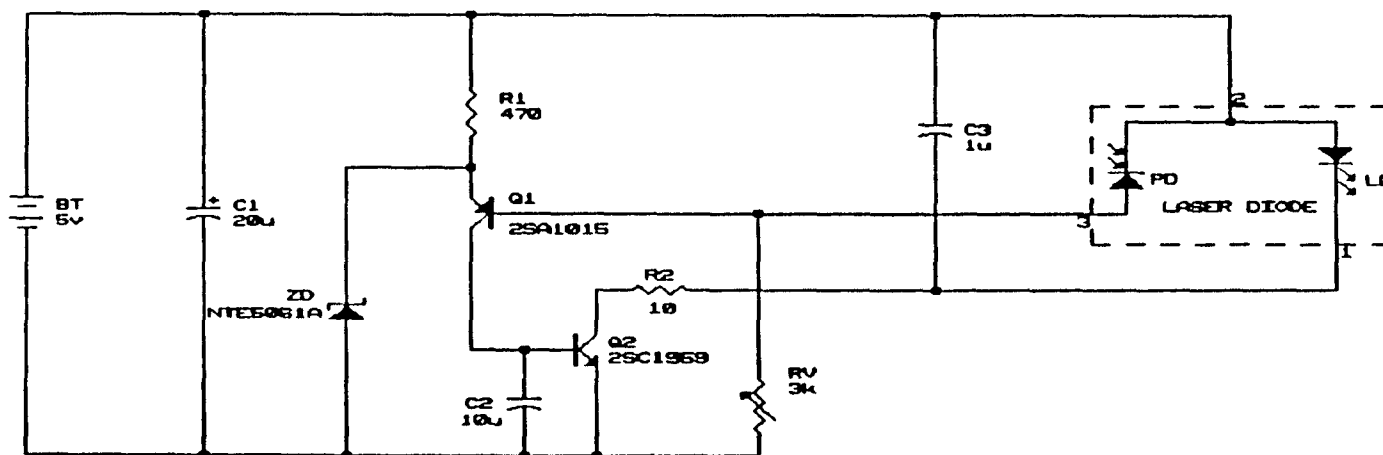
Laser Diode Control and Drive Circuit

B.1 Laser Diode Control and Drive Circuit

See Figure B.1

B.2 Circuit Devices List

See Table B.1.



New Jersey Institute of Technology		
Title Laser Diode and Control Circuit		
Size	Document Number	REV
A	SRP 000-88-4305-1	
Date:	October 12, 1990	Sheet of

Figure B.1: Laser Diode Control and Drive Circuit

<i>Device Name</i>	<i>Symbol</i>	<i>Unit</i>	<i>Values</i>	<i>Other</i>
Battery	BT	v	5.0	
Capacitance	C1	μ	20	
Zener Diode	ZD	v	2.4	NTE 5061A
Resistance	R1	Ω	470	
Transistor	Q1		2SA1015	NTE 290A
Transistor	Q2		2SC1959	NTE 85
Capacitance	C2	μ	10	
Resistance	R2	Ω	10	
Adjustable Resistance	RV	k Ω	3	
Capacitance	C3	μ	1	
Laser Diode	PD, LD			TOSHIBA TOLD 9200

Table B.1: Circuit Device list

Appendix C

Laser to Fiber Source Coupler Operation Principle

The source coupler utilizes the properties of lenses in combination with a novel tilt method to achieve submicron resolution. The method is based on precision control of the angle between the laser beam and receiver lens. The source coupler is comprised of two baseplates each having axial bore. One of the baseplates is adapted to receive a lens holder carries a lens and a fiber. The other baseplate is attached onto the laser. A resilient member such as a rubber O-ring is sandwiched between the baseplates. Threaded screws interconnect the two baseplates. The screws can then be adjusted by a screwdriver to alter the angular orientation of one baseplate relative to the other. The fiber output is monitored as the screws are adjusted until the detected output is optimized. The effects of angular misalignment are shown in Figure B.1. If the lens is tilted by an angle θ relative to the laser beam, the focused laser spot on the focal plane of the lens will be displaced relative to the receiver lens axis by an amount given by the equation $Z = f \tan \theta$, where f is the focal length of the lens. For 80 TPI screws, a lens with 1 mm focal length, and 20 mm lever arm = 0.1micron.

The tilt angle is changed until the focused laser beam spot overlaps with the receiver fiber core. The coupler could also be used as variable attenuator by merely offsetting the focused beam with respect to the fiber core. In addition, this method also reduces the light coupled back to the laser cavity. This is done by placing the fiber off-center with respect to lens axis which will result in non-zero tilt angle between the laser beam and the lens axes.

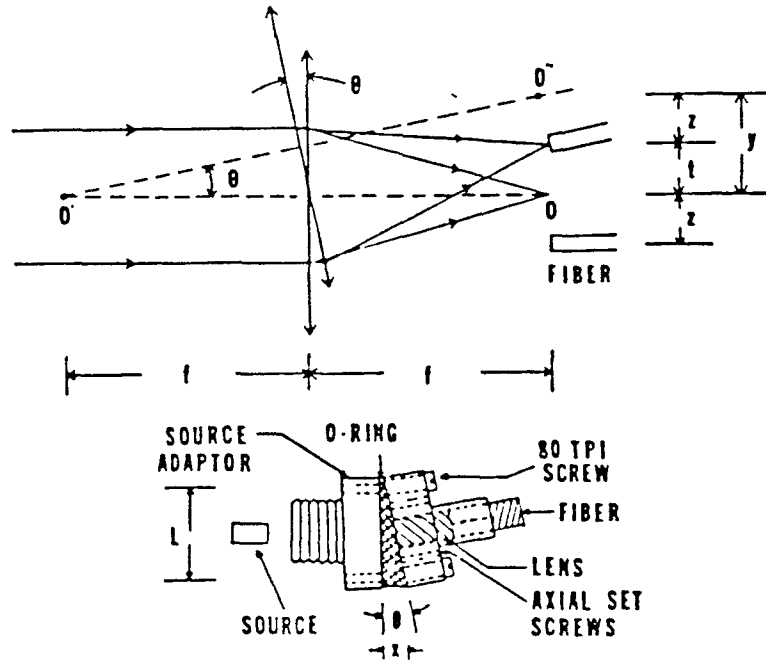


Figure C.1: Operation Principle of Axially Tilt Adjustable Components: For small tilt angles (θ), $z = t = f\theta$, $y = 2f\theta$, $\theta = x/L$

Appendix D

Photodetector AF65-R2F Technical Data

D.1 Features

The Ax65-R2F is a high quality low cost silicon photodiode specially designed for fiber optic applications operating in the 850 nm range. Frequency response of 100 MHz can be attained when used with maximum reverse bias voltage.

The photodiode is mounted in an hermetically sealed three pin TO-18 equivalent header with a low profile can. The cap contains a specially designed aperture facilitating easy and accurate fiber attachment and positioning. The photodiode active area of 1mm^2 is larger than the aperture so that a diverging light beam emanating from the fiber is intercepted to a maximum degree. The chip is precisely centered and is positioned very close to the window. The photodiode is also electrically isolated from the case.

D.2 Absolute Maximum Ratings

- Storage Temperature: $-55^{\circ}\text{to} + 125^{\circ}\text{C}$
- Operating Temperature: $-55^{\circ}\text{to} + 120^{\circ}\text{C}$
- Active Element Dimensions: $1\text{mm} \times 1\text{mm}$
- Window Diameter: 0.8 mm
- Chip to Window Spacing: 0.2 to 0.7 mm
- Recommended Wavelength Range: 400 nm to 1000 nm
- High Frequency Response: up to 100 MHz

D.3 PIN Connection

See Figure D.1.

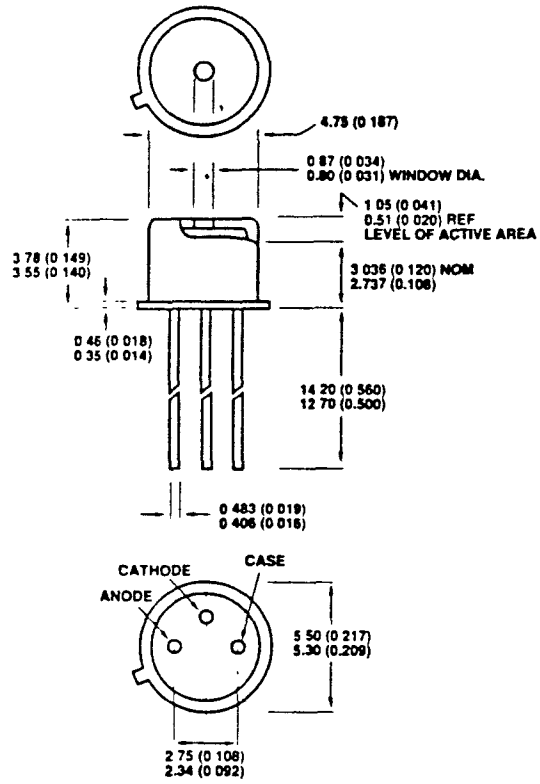


Figure D.1: PIN Connection

ELECTRO-OPTICAL CHARACTERISTICS*	MIN	TYPICAL	MAX	UNITS
Peak Sensitivity			850	nm
Operating Voltage			30	V
Peak DC Current			10	mA
Peak Pulse Current (1μs 1% duty cycle)			200	mA
Output Current Temperature Coefficient		0.15		%/°C
Responsivity at 900nm	0.52	0.55		A/W
Risetime at 900nm (10% to 70%) (Vr = 20V)		2.5		ns
Capacitance (Vr = 0V)		15		pF
Capacitance (Vr = 20V)		3.5		pF
Dark Current (Vr = 20V)			5	nA
Noise Equivalent Power at 900nm (Vr = 20V)		3.3×10^{-14}		W/Hz ^{1/2}

* All the parameters are characteristic of a photodiode operating at 23 °C, and connected to a load resistance of 50ohms (where appropriate)

Table D.1: Electro-Optical Characteristics

D.4 Electro-Optical Characteristics

See Table D.1.

Appendix E

Analog Amplifier and Filter Circuit

E.1 Analog Amplifier and Filter Circuit

See Figure E.1.

E.2 Circuit Devices List

See Table E.1.

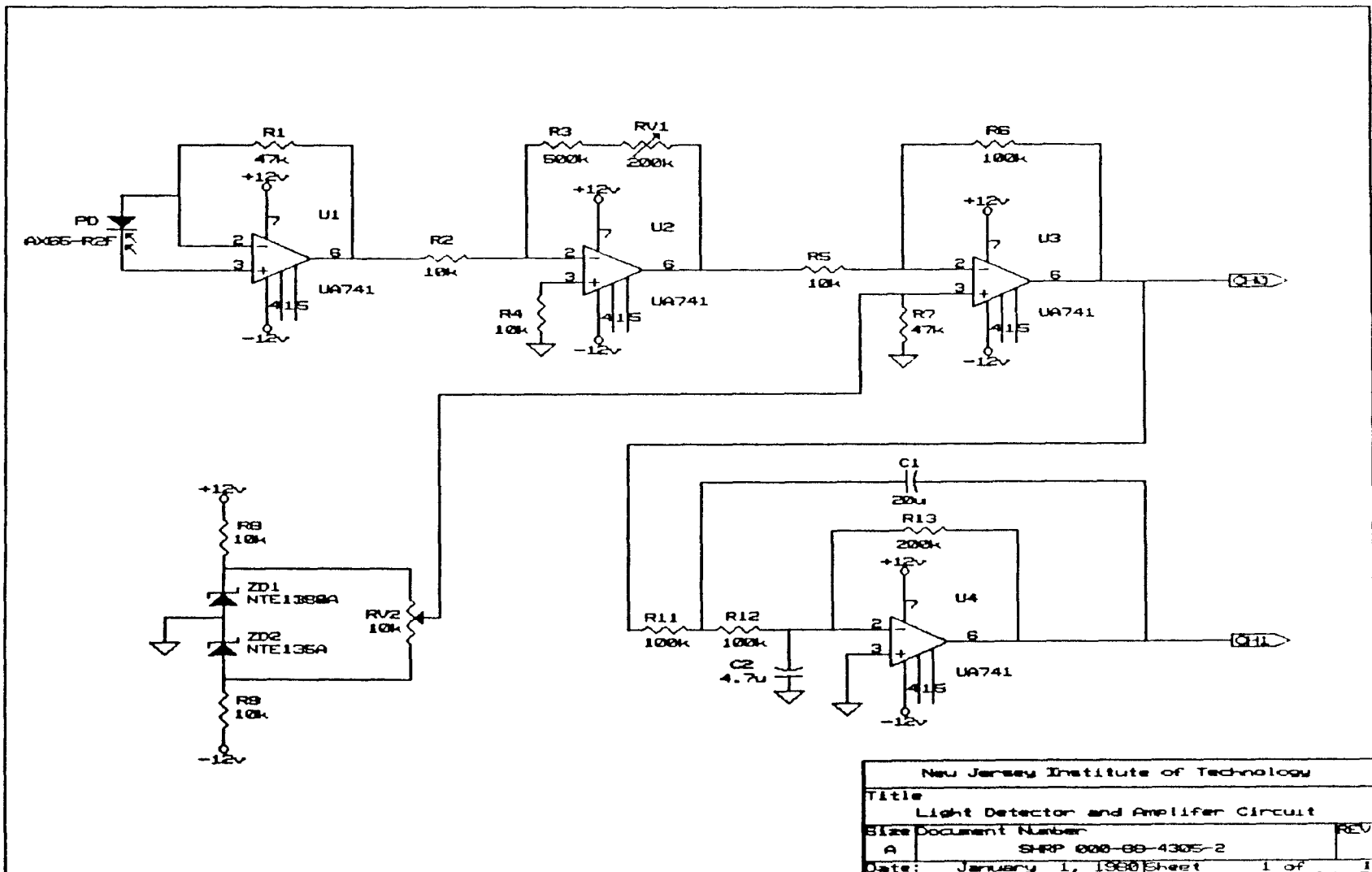


Figure E.1: Analog Amplifier and Filter Circuit

<i>Device Name</i>	<i>Symbol</i>	<i>Unit</i>	<i>Values</i>	<i>Other</i>
Photodiode	PD		AX65-R2F	Centronic Inc. NTE135A
Operational Amp.	U1-U4		UA741CP	
Zener Diode	ZD1, ZD2	v	5.1	
Resistance	R1, R7	k Ω	47	
Resistance	R2, R4, R5, R8, R9, R10	k Ω	10	
Resistance	R6, R11, R12	k Ω	100	
Resistance	R3	k Ω	500	
Resistance	R13	k Ω	200	
Capacitance	C1	μ	20	
Capacitance	C2	μ	4.7	
Adjustable Resistance	RV1	k Ω	0-200	
Adjustable Resistance	RV2	k Ω	0-50	

Table E.1: Circuit Device List

Appendix F

Program List

F.1 Signal Processing Program List

- Lotus 123 (Macro) Program Name: CT.WK1
- Input Reference Air Data File Name: D1.WK1
- Input Reference Concrete Data File Name: D2.WK1
- Input Test Data File Name: D3.WK1
- Output: Test Result and Plot of Reflected Light Intensity versus Time

F.2 The Size and Numbers of Air Bubbles Processing Program List

- Lotus 123 (Macro) Program Name: CN.WK1
- Input Test Data File Name: D3.WK1
- Output: Air Bubble Numbers in The Divided Range

```

File Name: CT.WK1      /wdcc1.r304`
                        {goto}c1`
Macro File Name: \d    /find1.wk1`
                        {goto}f4`
                        @avg(e4)`
                        {goto}g1`
                        /find2.wk1`
                        {goto}j4`
                        @avg(i4)`
                        {goto}k1`
                        /find3.wk1`
                        {goto}n4`
                        @abs(l4)`
                        /cn4`n5.n304`
                        {goto}o4`
                        @if((n4-m4)>0,n4,m4)`
                        /co4`o5.o304`
                        {goto}p4`
                        +o4-m4`
                        /cp4`p5.p304`
                        {goto}q4`
                        (+p4+p5)/2`
                        /cq4`q5.q304`
                        {goto}r4`
                        @sum(q4.q304)`
                        {goto}r5`
                        +r4*0.0333*10/(+f4-j4
                        /rff2`r5`
                        /rff0`k4.k304`
                        /gxk4.k304`
                        ao4.o304`
                        odar5`rqqv`

```

```

File Name. CN.WK1      {goto}c1`
                        /find3.wk1
Macro File Name: \d    {goto}f1
                        @abs(d4)
                        /cf4`f5`f304
                        {goto}g1`
                        @if(f4-e4>0,f4,e4)`
                        /cg4`g3.g304`
                        {goto}h4
                        +g4-e4`
                        /ch4`h5.h304
                        {goto}i4
                        @if(h4>0=and=h4<0.05,1,0)`
                        /ci4`i5.i304`
                        {goto}j3`
                        @sum(i4.i304)
                        {goto}j2
                        V.V.S.A.
                        {goto}j4
                        @if(h4>=0.05=and=h4<0.075,1,0)`
                        /cj4`j5.j304`
                        {goto}j3`
                        @sum(j4.j304)`
                        {goto}j2
                        V.S.A.`
                        {goto}k4`
                        @if(h4>=0.075=and=h4<0.1,1,0)
                        /ck4`k5.k304`
                        {goto}k3`
                        @sum(k4.k304)`
                        {goto}k2`
                        S.A.`
                        {goto}l4`
                        @if(h4>=0.1=and=h4<0.15,1,0)`
                        /cl4`l5.l304`
                        {goto}l3`
                        @sum(l4.l304)`
                        {goto}l2`
                        M.A.
                        {goto}m4
                        @if(h4>=0.15=and=h4<0.2,1,0)
                        /cm4`m5.m305`
                        {goto}m3
                        @sum(n4.m304)
                        {goto}m2
                        L.A.
                        {goto}n4`
                        @if(h4>0.2,1,0)`
                        /cn4`n5.n304
                        {goto}n3
                        @sum(n4.n304)`
                        {goto}n2`
                        V.L.A.

```

Appendix G

FFT Program List

- Input File Name: MODEL.OUT
- Output File Name: SYP.WK1


```

C      INTEGER I,NY
      REAL Y(16384),W(16384),PSE(16384),YSK
      COMPLEX YY(16384)
      CHARACTER*25 FILENAME, PSFILE
      PI=3.1415926
      OPEN(3,FILE='MODEL.OUT')
      DO 30 J=1,500
5      READ(3,*,ERR=17,END=905)TIME,Y(J)
16     GOTO 18
17     GOTO 5
18     IF((TIME EQ 0.000) AND (Y(J) EQ 0.000))GOTO 5
      IF (TIME .GE. 9 9998) GOTO 40
30     CONTINUE
40     WRITE(*,*) ' '
      WRITE(*,*) '!!!!!!!!!!!!!!!!!!!!!!!!!!!!!!'
      WRITE(*,*) 'THIS PROGRAM COMPUTES THE SPECTRUM'
      WRITE(*,*) '!!!!!!!!!!!!!!!!!!!!!!!!!!!!!!'
      WRITE(*,*) ' '

C
      M=12
      NPTS=256
      NFFT=2**M
      CALL WINDOW(W,NPTS,4)

C
C...REMOVE MEAN AND ZERO PADDING
C
      SCALE=1.0
      CALL ZOMEAN(Y,NPTS,AVF,SCALE)

C
      DO 500 K=1, NPTS
        YY(K)=CMPLX(Y(K)*W(K),0.)
500     CONTINUE
C
      DO 600 I=NPTS+1, NFFT
        YY(I)=CMPLX(0.,0.)
600     CONTINUE
      CALL NINFFT(YY,M,1)
      NY=1
      DO 610 I=1,NFT1/2+1
610     PSE(I)=CABS(YY(I))
      CCCCCCCCCCCCCCCCCCCCCCCCCCCCCCCCCCCCCCCCCCCCCCCCCCCCCCCCCC
C
      FILENAME='SYP.Wk1'
      OPEN(UNIT=10,FILE=FILENAME)
      DO 900 I=1, NFFT/2+1
        WRITE(10,*) PSE(I)
900     CONTINUE
      CLOSE(UNIT=10,STATUS='KEEP')
905     STOP
      END

CCCCCCCCCCCCCCCCCCCCCCCCCCCCCCCCCCCCCCCCCCCCCCCCCCCCCCCCCCCC
CC      SUBROUTINE ZOMEAN (2/23/88)
CC
CC      USAGE: (ALL ZOMFAN(X,NPTS,AVE,SCALE)
CC
CC      X- INPUT ARRAY
CC      AVE- AVERAGE OF THE INPUT ARRAY
CC      SCALE- SCALING FOR THE OUTPUT
CC
CCCCCCCCCCCCCCCCCCCCCCCCCCCCCCCCCCCCCCCCCCCCCCCCCCCCCCCCCCCC
      SUBROUTINE ZOMEAN(X,NPTS,AVE,SCALE)
      REAL X(1), AVE, SCALE
      INTEGER NPTS

C
      SUM=0.0
      DO 10 I=1, NPTS
        SUM=SUM+X(I)
10     CONTINUE
C
      AVE=SUM/FLOAT(NPTS)
      DO 20 I=1, NPTS
        X(I)=SCALE*(X(I)-AVE)
20     CONTINUE
C
      RETURN
      END

```

```

C
C SUBROUTINE ... WINDOW... GENERATES DIFFERENT WINDOWS
C
C USAGE: CALL WINDOW(W,N,IDGT)
C
C W- OUTPUT VECTOR OF DIMENSION N, WINDOW FUNCTION
C N- WINDOW LENGTH
C IDGT- TYPE OF WINDOWING FUNCTION
C      1. RECTANGULAR
C      2. BARTLETT
C      3. HANNING
C      4. HAMMING
C      5. BLACKMAN
C
C*****
SUBROUTINE WINDOW(W,N,IDGT)
REAL W(N)
PI=3.1415926
NHAF=N/2
C
WRITE(*,*) ' '
IF (IDGT.EQ.1) THEN
DO 10 I=1, N
W(I)=1.0
10 CONTINUE
GOTO 99
C
ELSEIF (IDGT.EQ.2) THEN
DO 20 I=1, NHAF
W(I)=2.*FLOAT(I-1)/FLOAT(N-1)
20 CONTINUE
DO 30 I=NHAF+1, N
W(I)=2.-2.*FLOAT(I-1)/FLOAT(N-1)
30 CONTINUE
GOTO 99
C
ELSEIF (IDGT.EQ.3) THEN
DO 40 I=1, N
ANG=2.*PI*FLOAT(I-1)/FLOAT(N-1)
W(I)=0.5*(1.-COS(ANG))
40 CONTINUE
GOTO 99
C
ELSEIF (IDGT.EQ.4) THEN
DO 50 I=1, N
ANG=2.*PI*FLOAT(I-1)/FLOAT(N-1)
W(I)=0.54-0.46*COS(ANG)
50 CONTINUE
GOTO 99
C
ELSEIF (IDGT.EQ.5) THEN
DO 60 I=1, N
ANG=2.*PI*FLOAT(I-1)/FLOAT(N-1)
W(I)=0.42-0.5*COS(ANG)+0.08*COS(2.*ANG)
60 CONTINUE
GOTO 99
C
ELSE
ENDIF
99 WRITE(*,*) ' '
RETURN
END

```

```

CCCCCCCCCCCCCCCCCCCCCCCCCCCCCCCCCCCCCCCCCCCCCCCCCCCCCCCCCCCC
C      SUBROUTINE NINIFT
C
C      CALCULATES THE DISCRETE FAST FOURIER TRANSFORM OR
C      THE INVERSE DISCRETE FAST FOURIER TRANSFORM
C      USING BUTTERFLY-IN-FREQUENCY SCHEMATA
C
C      USAGE: CALL NINIFT(X,M,SIGN)
C
C      ARGUMENTS:
C      X=COMPLEX ARRAY OF DIMENSION *
C      M=INTEGER (M=2**N)
C      SIGN=1 PERFORM FAST FOURIER TRANSFORM
C      SIGN=-1 PERFORM INVERSE FAST FOURIER TRANSFORM
C
C      REMARKS: X(N-i+1) = C.C. OF X(i+1) FOR i=1-->N/2-1
C              i.e., X(1)-->X(N/2+1) (CORRELATION) 0-->PI
C
C      SUBROUTINE REQUIRED : NONE
C
CCCCCCCCCCCCCCCCCCCCCCCCCCCCCCCCCCCCCCCCCCCCCCCCCCCCCCCCCCCC
SUBROUTINE NINIFT(X,M,SIGN)
COMPLEX X(1), U, W, T
INTEGER LE1,LE,SIGN
N=2**M
PI=3.14159265358979
C...CHECK IF PERFORMING INVERSE FFT
IF (SIGN.EQ.1) GO TO 5
DO 1 I=1,N
X(I)=X(I)/FLOAT(N)
1 CONTINUE
C
5 DO 20 L=1,M
LE=2**(M+1-L)
LE1=LE/2
U=CMPLX(1.0,0.0)
W=CMPLX(COS(PI/FLOAT(LE1)),-SIGN*SIN(PI/FLOAT(LE1)))
DO 10 J=1, LE1
DO 10 I=J, N, LE
IP=I+LE1
T=X(I)+X(IP)
X(IP)=(X(I)-X(IP)) * U
X(I)=T
10 CONTINUE
U=1-W
20 CONTINUE
NV2=N/2
NM1=N-1
J=1
DO 30 I=1,NM1
IF(I.GE.J) GO TO 25
T=X(J)
X(J)=X(1)
X(1)=T
25 K=NV2
26 IF(K.GE.J) GO TO 30
J=J-K
K=K/2
GO TO 26
30 J=J+K
C
WRITE(1,4) * *
WRITE(1,5) '!!! RETURN FROM SUBROUTINE NINIFT !!!'
RETURN
END

```